

# Monitoring and modeling seasonally varying anthropogenic and biogenic $CO_2$ over a large tropical metropolitan area

Rafaela Cruz Alves Alberti<sup>1</sup>, Thomas Lauvaux<sup>3</sup>, Angel Liduvino Vara-Vela<sup>6,7,8</sup>, Ricard Segura Barrero<sup>2</sup>, Christoffer Karoff<sup>6,7,8</sup>, Maria de Fátima Andrade<sup>1</sup>, Márcia Talita Amorim Marques<sup>1</sup>, Noelia Rojas Benavente<sup>5</sup>, Osvaldo Machado Rodrigues Cabral<sup>4</sup>, Humberto Ribeiro da Rocha<sup>1</sup>, and Rita Yuri Ynoue<sup>1</sup>

<sup>1</sup>Department of Atmospheric Sciences, University of São Paulo, Brazil

<sup>2</sup>Institute of Environmental Sciences and Technology, Universitat Autònoma de Barcelona, Spain.

<sup>3</sup>Université de Reims Champagne-Ardenne, CNRS, GSMA, Reims, France

<sup>4</sup>Brazilian Agricultural Research Corporation, Embrapa Environment, Brazil

<sup>5</sup>Physics Institute, University of São Paulo, Brazil

<sup>6</sup>Department of Geoscience, Aarhus University, Denmark

<sup>7</sup>Department of Physics and Astronomy, Aarhus University, Aarhus, Denmark

<sup>8</sup>iCLIMATE Aarhus University Interdisciplinary Centre for Climate Change, Aarhus, Denmark

**Correspondence:** Rafaela Cruz Alves Alberti (rafaela\_alves@usp.br)

**Abstract.** Atmospheric  $CO_2$  concentrations in urban areas reflect a combination of fossil fuel emissions and biogenic fluxes, offering a potential approach to assess city climate policies. However, atmospheric models used to simulate urban  $CO_2$  plumes face significant uncertainties, particularly in complex urban environments with dense populations and vegetation. This study addresses these challenges by analyzing  $CO_2$  dynamics in the Metropolitan Area of São Paulo (MASP) using the Weather Research and Forecasting model with Chemistry (WRF-Chem). Simulations were evaluated against ground-based observations from the METROCLIMA network, the first greenhouse gas monitoring network in South America, and column concentrations ( $XCO_2$ ) from the OCO-2 satellite spanning February to August 2019. To improve biogenic fluxes, we optimized parameters in the Vegetation Photosynthesis and Respiration Model (VPRM) using eddy covariance flux measurements for key vegetation types, including the Atlantic Forest, Cerrado, and sugarcane. Results show that at the urban site (IAG), the model consistently underestimated  $CO_2$  concentrations, with a negative mean bias of -9 ppm throughout the simulation period, likely due to the complexity of vehicular emissions and urban dynamics. In contrast, at the vegetated site (PDJ), simulations showed a consistent positive mean bias of 5 ppm and closely matched observations. Seasonal analyses revealed higher  $CO_2$  concentrations in winter, driven by greater atmospheric stability and reduced vegetation uptake estimated by VPRM, while summer exhibited lower levels due to increased mixing and higher agricultural productivity. A comparison of biogenic and anthropogenic scenarios highlights the need for integrated emission modeling and improved representation of biogenic fluxes, anthropogenic emissions, and boundary conditions for high-resolution modeling in tropical regions.

18 Urban areas, although occupying only a small fraction of the Earth’s surface, exert an outsized influence on global carbon  
19 emissions. Accounting for a staggering 70% of  $CO_2$  emissions from fossil fuel burning while covering just 2% of the planet’s  
20 landmass (Seto et al., 2014; Change et al., 2014), cities have become focal points for climate action. The relentless pace of  
21 urbanization has further exacerbated this phenomenon, driving up energy consumption and emissions levels (Seto et al., 2012).  
22 Consequently, combating climate change necessitates a targeted approach, with policies increasingly tailored to address urban  
23 emissions. In response to the growing need for climate action, initiatives like the International Council for Local Environmen-  
24 tal Initiatives (ICLEI), the C40 Cities Climate Leadership Group (C40), and the Covenant of Mayors (CoM) have emerged  
25 to coordinate global efforts and share best practices among cities. These initiatives highlight the crucial role cities play in the  
26 fight against climate change and the importance of localized mitigation strategies. São Paulo, Brazil’s largest municipality  
27 (IBGE, 2021), is a member of C40 and focuses on reducing greenhouse gas emissions, with transportation accounting for  
28 58% of its total emissions (SEEG, 2019). The city is working towards carbon neutrality through projects in green infrastruc-  
29 ture, urban planning, public transportation improvements, energy efficiency, and waste management (Caetano et al., 2021).  
30 These efforts aim to reduce emissions and enhance São Paulo’s resilience, fostering a more sustainable urban environment.  
31 Central to these efforts is the need for accurate data and robust modeling frameworks to inform policy decisions effectively.  
32 Urban atmospheric networks, such as MASP, in Brazil, provide vital insights into greenhouse gas concentrations and emission  
33 patterns. By leveraging these datasets alongside sophisticated atmospheric transport models and statistical techniques, policy-  
34 makers gain tools for designing targeted interventions and monitoring their efficacy. However, the complexity of urban  $CO_2$   
35 dynamics presents significant challenges for modeling and analysis. Process-driven biosphere models and inverse modeling  
36 techniques offer complementary approaches for capturing the intricate spatio-temporal variabilities inherent in urban environ-  
37 ments (Kaiser et al.; Che et al., 2022; Zhang et al., 2023; Wilmot et al., 2024). Despite advancements in modeling capabilities,  
38 gaps remain in our understanding of  $CO_2$  dynamics, particularly at regional and national scales. South America, in particu-  
39 lar, suffers from limited data availability, and research focusing on this region is scarce. Additionally, vegetation models in  
40 tropical regions often exhibit poor performance due to inaccuracies in simulating seasonality, oversimplified representations  
41 of biodiversity, and errors in carbon and water cycle interactions. These models struggle to capture the complex dynamics  
42 of tropical ecosystems, leading to underestimations of productivity and poor predictions of vegetation responses to climate  
43 variability (De Pue et al., 2023; He et al., 2024). This study aims to address these gaps by conducting a comprehensive analysis  
44 of anthropogenic and biospheric  $CO_2$  dynamics near the MASP. To achieve this, we employed the WRF-Chem model, offline  
45 coupled with the VPRM model (Mahadevan et al., 2008). Vehicular emissions were incorporated using the Vehicle Emission  
46 Inventory model (VEIN) (Ibarra-Espinosa et al., 2018), while emissions from the industrial, energy, residential, and refinery  
47 sectors were derived from the EDGAR inventory. This integrated modeling framework enables a detailed assessment of the  
48 main drivers of  $CO_2$  variability in the region. In addition, we utilized data from the OCO-2 satellite to cover the study domain,  
49 comparing WRF-Chem-simulated  $XCO_2$  concentrations (considering biogenic and anthropogenic emissions) post-processed  
50 using OCO-2 averaging kernels (i.e., smoothed  $XCO_2$ ). Through a combination of model simulations, field observations, and

satellite data analysis, this study seeks to provide an understanding of  $CO_2$  dynamics in urban environments. This is the first study in this field conducted in any city in the Global South, making it an innovative effort with significant implications. By setting a precedent, this research paves the way for future studies, contributing to a more comprehensive global picture of  $CO_2$  dynamics in urban environments.

## 2 WRF-Chem

### 2.1 Model set-up

A set of high-resolution simulations of atmospheric Greenhouse Gas concentrations were performed with the WRF-Chem model version 4.0. The WRF-Chem was used to simulate the transport of the mole fraction of  $CO_2$ , and no chemical processes or reactions have been used. The period simulated was from 1 February to 31 August 2019. This period was selected due to available data from monitoring stations from the METROCLIMA network for  $CO_2$ . The simulations were made for each month. For each run, the simulation was initiated 5 days before and these 5 days were discarded as spin-up time. The single modeling domain was centered at 23.5°S and 46.3°W with a horizontal grid spacing of 3 km as shown in Figure 1, projected on a Lambert plane and consists of 166 grid points in the west-east direction, 106 grid points in the north-south direction, and 34 vertical levels that extend from the surface up to 50 hPa (20 km), as used in previous studies for this same area (Andrade et al., 2015; Vara-Vela et al., 2016; Gavidia-Calderón et al., 2023; Benavente et al., 2023). The meteorological conditions used to drive the simulations were obtained from the European Centre for Medium-Range Weather Forecasts (ECMWF) ERA5 reanalysis dataset, with a horizontal resolution of  $0.25^\circ \times 0.25^\circ$  and 6-hourly intervals (Hersbach, 2016). For  $CO_2$ , initial and boundary conditions were provided by Carbon Tracker, which offers data at a horizontal resolution of  $3^\circ$  in longitude and  $2^\circ$  in latitude, with 25 vertical layers (<http://carbontracker.noaa.gov>). This global dataset was interpolated to provide lateral boundary conditions for the simulations and ensure consistency with the WRF-Chem. The main physics and chemistry options used in this study are listed in Table 1.

#### 2.1.1 Anthropogenic Emissions

In the MASP, the vehicular fleet is the primary source of  $CO_2$  emissions (CETESB, 2019). For this study, we employed the VEIN model, a tool designed to estimate emissions from mobile sources. VEIN accounts for both exhaust and evaporative emissions performs speciation, and includes functions to generate and spatially allocate emissions databases (Ibarra-Espinosa et al., 2018). The model enables the use of customized emission factors, which in this study were derived from experimental campaigns conducted in traffic tunnels within São Paulo (Nogueira et al., 2021). VEIN processes vehicle fleet age distributions extrapolates hourly traffic data, and estimates emissions with high temporal and spatial resolution. For consistency with the WRF-Chem model domain, VEIN emissions were aggregated to a 3 km spatial resolution. Additionally, we included Figure B1 in Appendix B, which illustrates the spatial distribution of average daily  $CO_2$  emissions for August 2019, the total monthly emissions from February to August, and the diurnal profile of vehicular  $CO_2$  emissions as estimated by the VEIN model.

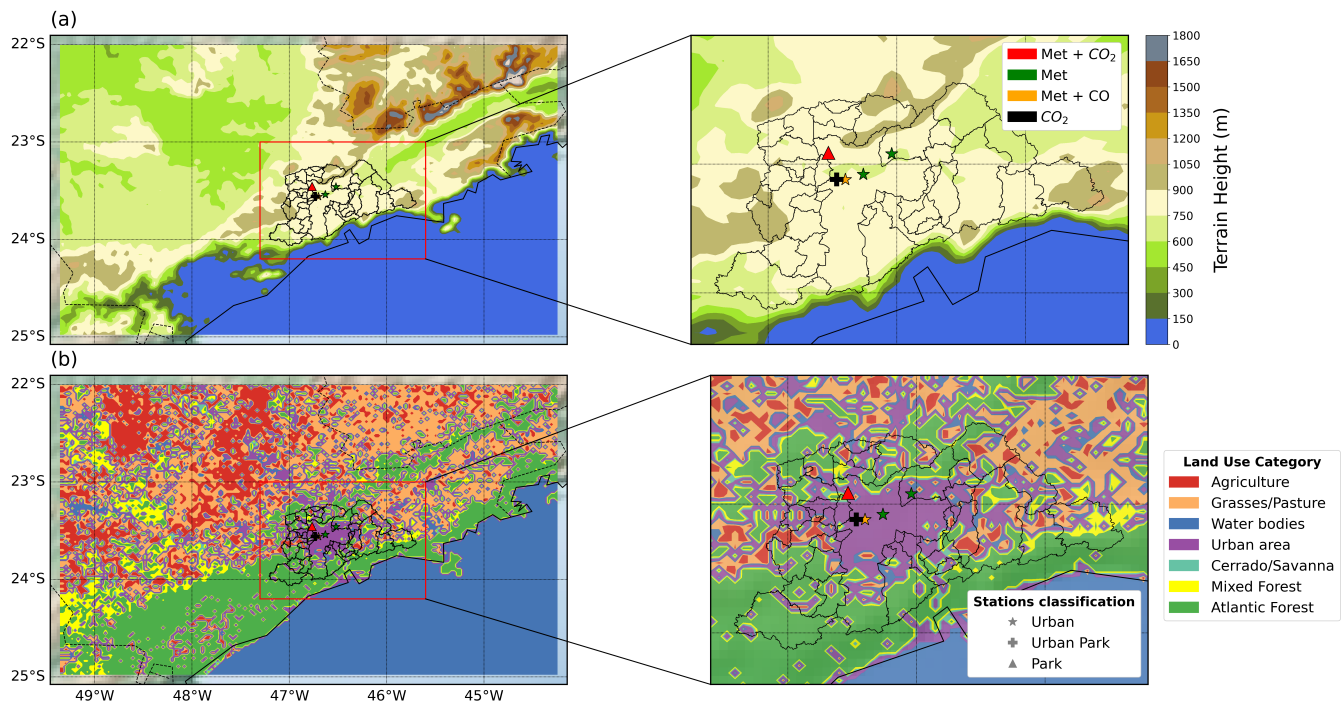


**Figure 1.** Panel (a) shows the terrain height and urban boundaries of the MASP region within the WRF-Chem model domain (D01). Station classifications are indicated using different symbols: Urban (★), Urban Park (⊕), and Park (▲). Panel (b) presents the land use category map for the same domain (D01), which was used by the VPRM model to calculate  $CO_2$  fluxes. The colors of the station markers represent the type of measurements conducted at each location: red indicates stations measuring both meteorological variables (Met) and  $CO_2$  concentrations; green indicates stations measuring only Met; dark yellow denotes stations measuring both Met and CO concentrations; and black indicates stations measuring only  $CO_2$  concentrations. The IAG station is marked as (⊕), the PDJ station is (▲), Pinheiros station is (★), Guarulhos and Parque D. Pedro II are (★).

Emissions from the industry, refineries, residential, and energy sectors were obtained from the EDGAR v6.0 GHG inventory for 2018 (Crippa et al., 2021). EDGAR provides global annual emissions at  $0.1^\circ \times 0.1^\circ$  spatial resolution, which we regridded to 3 km using bilinear interpolation to match the WRF-Chem model domain. EDGAR does not provide hourly temporal profiles, these emissions were assumed constant over the day (Figure B2 in Appendix B). To evaluate the relative contribution of each sector to total emissions in the MASP, Figure B3 (Appendix B) presents the average daily  $CO_2$  emissions in August 2019. Transport emissions represented the dominant share, accounting for 76.1%, followed by industry (10.0%), refineries (7.6%), residential (3.8%), and energy (2.5%) sectors.

### 2.1.2 Biogenic Fluxes

Biogenic  $CO_2$  fluxes were simulated offline using the VPRM model (Mahadevan et al., 2008) and incorporated as flux input data in the WRF-Chem simulations. This model estimates net ecosystem exchange (NEE) by calculating the difference between



**Table 1.** WRF-Chem Simulation Design.

Atmosphere Schemes		
Scheme	Type	Description/Reference
Microphysics	Two-moment	Morrison scheme (Morrison et al., 2009)
Longwave radiation	RRTMG	(Iacono et al., 2008)
Shortwave radiation	RRTMG	(Iacono et al., 2008)
Boundary layer	YSU	(Hong et al., 2006)
Land surface	Noah LSM	Unified scheme (Tewari et al., 2007)
Initial and Lateral Boundary Conditions		
Meteorological	ERA5	0.25°, 34 pressure levels
$CO_2$	Carbon Tracker	25 vertical layers
Emissions Inventories/Model		
Anthropogenic	EDGAR v6.0	(Crippa et al., 2021) and VEIN (Ibarra-Espinosa et al., 2018)
Biogenic	VPRM	(Mahadevan et al., 2008)

gross ecosystem exchange (GEE) and ecosystem respiration (R), where negative fluxes indicate  $CO_2$  absorption by ecosystems (Equation 1).

$$NEE = GEE - R \tag{1}$$

The meteorological variables 2m air temperature ( $T_{2m}$ ) and downward shortwave radiation (PAR) from WRF model simulations were used to calculate the GEE (Equation 2) and Respiration (Equation 3) fluxes. Additionally, factors such as the light use efficiency ( $\lambda$ ), PAR saturation (PAR0), and the Enhanced Vegetation Index (EVI), which refer to the fraction of shortwave radiation absorbed by leaves were used to calculate GEE. The temperature sensitivity of the photosynthesis parameter (Tscale) and the effects of leaf age on canopy photosynthesis parameter (Pscale) were both calculated as functions of the land surface water index (LSWI) to identify the green-up (leaf expansion) and senescence phases (Mahadevan et al., 2008). These vegetation indices were derived from Moderate Resolution Imaging Spectroradiometer (MODIS) reflectance data from MOD09A1 Version 6 (Vermote, 2021).

$$GEE = \lambda \times T_{scale} \times P_{scale} \times W_{scale} \times EVI \times \frac{1}{1 + \frac{PAR}{PAR_0}} \times PAR \tag{2}$$

Respiratory fluxes (R) were estimated using a linear model based on air temperature and two parameters that represent the linear sensitivity of respiration to air temperature ( $\alpha$ ) and the baseline respiration ( $\beta$ ), as defined in Mahadevan et al. (2008).

106

$$R = \alpha \times T_{2m} + \beta$$

(3)

107

The land cover data used by the VPRM were derived from the MapBiomass data (Souza Jr et al., 2020). The VPRM parameters ( $\lambda$ ,  $PAR_0$ ,  $\alpha$ ,  $\beta$ ) were optimized against flux tower NEE for the main land cover type over the study domain described in section 2.2.2.

109

110

### 2.1.3 Meteorological data

111

Meteorological data from the São Paulo State Environmental Protection Agency (CETESB) air quality network were used to evaluate the model’s performance in simulating meteorological fields. CETESB manages automatic and manual air quality stations over São Paulo state. These stations provide hourly information on meteorological and pollutant parameters, such as air temperature, wind speed, and wind direction (Table 2), as well as the concentration of air pollutants. Monitoring follows instrumentation standards and directives from the Environmental Protection Agency (US EPA) and the World Health Organization (WHO) respectively for air pollutants, and from the World Meteorological Organization (WMO) for meteorological variables (CETESB, 2019). The air quality and meteorological data are continuously published on the Qualar website (<https://qualar.cetesb.sp.gov.br/qualar/>). This study used data from four stations located in the MASP (Figure 1): Parque D. Pedro II, PDJ, Guarulhos, and Pinheiros. Table 2 provides the location of the sites, the classification type of the stations, the observed variables, and the data source.

120

**Table 2.** Location of the sites used for the model evaluation of the meteorological drivers, together with a list of the meteorological variables included in the analysis.

Sites	Location	Classification	Variables	Source Data
Parque D.Pedro II	23.54S, 46.63W	Urban	$T_{2m}$ , WD, WS	CETESB
PDJ	23.45S, 46.76W	Park	$T_{2m}$ , WD, WS and $CO_2$	CETESB/ METROCLIMA
Guarulhos	23.46S, 46.52W	Urban	$T_{2m}$ , WD, WS	CETESB
Pinheiros	23.46S, 46.70W	Urban	$T_{2m}$ , WD, WS and CO	CETESB
IAG	23.55S, 46.73W	Urban Park	$CO_2$	METROCLIMA

Note: Air temperature at 2 m ( $T_{2m}$ ), wind speed (WS), and wind direction (WD).

121

## 2.2 CO<sub>2</sub> observational data

122

### 2.2.1 Ground-based observations

123

We assessed near-surface model performance using  $CO_2$  observations from the METROCLIMA network in São Paulo (see Table 3 and Figure 1), the first conventional in situ greenhouse gas measurement network established in South America ([www.metroclima.iag.usp.br](http://www.metroclima.iag.usp.br)). The network comprises four continuously operating monitoring stations, all located within the

125

MASP and equipped with cavity ring-down spectroscopy instruments (Picarro) that measure the concentrations of  $CO_2$  following the directives from WMO. The monitoring stations are located at various locations within MASP: in a vegetated area at the extreme west (Pico do Jaraguá, PDJ); in a suburban area in the center-west, inside the campus of the University of São Paulo (IAG); at the top of a 100 m building (ICESP); and in an urban area in the east zone characterized by heavy traffic in the neighborhood (UNICID). However, we only used data from the IAG and PDJ sites, which are 13 km apart, as these were the only two stations monitoring  $CO_2$  during the selected study period, prior to the Covid-19 pandemic (Souto-Oliveira et al., 2023).

**Table 3.** Description of the METROCLIMA monitoring stations utilized in this study.

Station	Instrument	Inlet elevation (m)	Altitude (m)
PDJ	G2301 II	3	1079
IAG	G2301 II	15	731

### 2.2.2 $CO_2$ fluxes data and VPRM optimization

In this study, the VPRM model computed the biosphere fluxes for 5 different plant functional types (PFT), representing different vegetation land covers, and for that required a set of four model parameters for each vegetation class, dependent on the region of interest. Ideally, these parameters are optimized using a network of eddy flux towers for each PFT over the domain. The VPRM parameters were optimized for only three PFT corresponding to the three ecosystems observed by eddy-covariance flux towers. However, these three PFT represent almost 60% of land covers over the domain (i.e. sugarcane - 23.86%, Atlantic Forest - 34.86%, and Cerrado - 0.91%). We used a set of parameters optimized by Botía et al. (2022) for the remaining PFT's, such as grasses and mixed forest, based on measurements from sites in the Amazon region in Brazil, deployed in the context of the Large Scale Biosphere-Atmosphere Experiment (LBA-ECO) (Botía et al., 2022). The methodology for optimizing the VPRM parameters for the Atlantic Forest used data from Serra do Mar State Park in São Paulo State, Brazil (23°17'S, 45°03'W at 900 m altitude) for the period from January 2015 to December 2015 (Freitas, 2012). For Cerrado, we used observed data from Pé Gigante, in São Paulo, Brazil (21°36'S, 47°34'W at 660m) from January 2015 to January 2017 (Rocha et al., 2002). For sugarcane we used data from the municipality of Pirassununga, in São Paulo State, Brazil (21°57'S, 47°20'W at 655 m altitude) for the period from November 2016 to August 2017 (Cabral et al., 2020). The VPRM parameters were optimized separately for each PFT using half-hourly observed fluxes from the flux towers over the entire observation periods. We optimized the parameters for the GEE and R simultaneously, and for the default VPRM parameters we used non-linear least squares minimization between the modeled NEE and the flux tower estimation of the observed NEE. In the optimization, the VPRM model is driven by the meteorological measurements of the sites and their specific land covers. The vegetation indices (EVI and LSWI) were derived from the product MOD09A1 of MODIS at 500 m resolution and 8-daily frequency using Google Earth Engine.

### 153 2.2.3 $XCO_2$ satellite observations

154 Satellite-based  $XCO_2$  observations were utilized in addition to surface  $CO_2$  measurements over the study domain. OCO-2,  
155 NASA's inaugural Earth remote sensing satellite dedicated to atmospheric  $CO_2$  observations, was launched in 2014 (Crisp,  
156 2015). Operating on a solar synchronous orbit, OCO-2 conducts global measurements of  $CO_2$  absorption and emission at 13:30  
157 Local Solar Time. The OCO-2 observation data utilized were ACOS L2 Lite Output Filtered with oco2-lite\_fle\_prefilter\_b9,  
158 which were converted from Level 1 radiance to Level 2 data using the ACOS retrieval algorithm developed by O'Dell et  
159 al. (2012). Data quality assessment for OCO-2 observations can be performed using the xco2\_quality\_flag and warn\_level  
160 parameters, as detailed in the OCO-2 Data Product User's Guide (Osterman et al., 2018). In this study, we considered only  
161 OCO-2 data with a '0' xco2\_quality\_flag value that indicates "good" quality. Initially, simulated  $CO_2$  concentrations were  
162 interpolated to match the latitude, longitude, horizontal resolution, and vertical levels of OCO-2 data. Additionally, to ensure  
163 consistency in the comparison, the simulated data were selected to correspond as closely as possible to the OCO-2 overpass  
164 time (13:30 Local Solar Time) over the study region. Due to the difference in data types and units between the simulated  
165  $CO_2$  concentrations and observed  $XCO_2$  from satellites, a conversion was necessary prior to comparison. Consequently,  $CO_2$   
166 concentrations simulated at each pressure level in the WRF-Chem were transformed into  $XCO_2$  concentrations following the  
167 methods by Connor et al. (2008) and O'Dell et al. (2012), as follows:

$$168 \quad XCO_2^{\text{model}} = XCO_{2a} + \sum_i w_i^T A_i (CO_2^{\text{interp}} - CO_{2a})_i \quad (4)$$

169 where  $XCO_{2a}$  is a priori  $XCO_2$ ,  $w_i^T$  is the pressure weighting function,  $A_i$  is the column averaging kernel,  $CO_2^{\text{interp}}$  is the  
170 interpolated simulated  $CO_2$  concentrations of WRF-Chem, and  $CO_{2a}$  is a priori  $CO_2$ .

### 171 2.3 Evaluation metrics

172 Several statistical metrics are available for assessing the effectiveness of atmospheric models. These include mean bias error  
173 (bias, Equation A1), indicating the average difference between the simulation and the observation; root-mean-square error  
174 (RMSE, Equation A2), which quantifies the square root of the average squared deviation between simulation and observation;  
175 and the correlation coefficient ( $R^2$ , Equation A3), representing the degree and direction of the linear connection between  
176 the simulation and the observation. To evaluate the model performance, we calculated the bias, RMSE, and  $R^2$ , with the  
177 corresponding equations provided in Appendix A.

## 178 3 Results

179 Hourly simulations were conducted from 1 February to 31 August 2019, with each month simulation including a five-day  
180 spin-up period. In the following sections, the performance of meteorological drivers will be first presented, followed by the  
181 terrestrial surface  $CO_2$  fluxes and atmospheric  $CO_2$  concentrations from the IAG and PDJ stations. These measurements were

182 used to evaluate the model performances and to assess the local impacts of the main  $CO_2$  sources and sinks on atmospheric  
183  $CO_2$  concentrations.

### 184 3.1 Model performance for meteorological drivers

185 The assessment of the meteorological model performances is essential for accurately simulating greenhouse gas concentrations.  
186 In this study, the model represented the temporal variability and trends of 2-meter temperature ( $T_{2m}$ ), 10-meter wind speed  
187 (WS), and direction (WD) throughout the simulation period, as illustrated in Figure 2 and the supplementary material. The  
188 WRF-Chem model effectively captured significant changes in the observed variables, although it failed to accurately represent  
189 the maximum and minimum peaks, particularly for wind speed. The simulated 2-meter temperature tended to overestimate  
190 values at specific sites, such as Parque D. Pedro II (bias =  $0.5^\circ C$ ), Guarulhos (bias =  $0.1^\circ C$ ) (see figure B4a and B5a in  
191 Appendix B), and PDJ (bias =  $0.7^\circ C$ ) (see Figure 2a). However, at the Pinheiros station, the simulated surface temperature was  
192 underestimated (bias =  $-0.7^\circ C$ ) (Figure B6a in Appendix B).

193 In terms of biases, the model overestimated the wind speed at all sites (bias  $< 1.5 \text{ ms}^{-1}$ ), with PDJ exhibiting the high-  
194 est mean bias ( $1.4 \text{ ms}^{-1}$ ). This overestimation could be attributed to the model's misrepresentation of land use, leading to  
195 elevated wind speeds in areas classified as urban rather than vegetated. Notably, numerical models tend to lack sensitivity  
196 in simulating very low-velocity speeds due to imperfections in land surface processes and the model's ability to accurately  
197 resolve topographical features (Shimada et al., 2011; Zhang et al., 2009; Vara-Vela et al., 2018, 2021). The model's wind  
198 directions showed sufficient sensitivity, aligning accurately with observed values. Both the model and observations indicated  
199 that prevailing winds were predominantly from the southeast. In summary, the WRF model showed proficiency in reproducing  
200 atmospheric conditions in the study area, particularly concerning air temperature and wind direction, with similar performances  
201 as previous studies (Feng et al., 2016; Deng et al., 2017).

### 202 3.2 The VPRM Model: Evaluation with Flux Tower Data

203 The optimization results are shown in Table 4. Substituting alpha and beta back into the respiration equation led to a better  
204 model representation of NEE compared to NEE values simulated with default parameters (Mahadevan et al., 2008) for the  
205 main PFT across the domain.

206 The optimized VPRM parameters for the Atlantic Forest exhibited the greatest discrepancies compared to other vegetation  
207 classes. The geomorphological characteristics of the Atlantic forest differ from those of the evergreen forest studied by (Ma-  
208 hadevan et al., 2008), where the default parameters (VPRM\_default, represented by the red curve in Figure 3) were used. The  
209 optimized VPRM parameters (VPRM\_optimized, shown as the green curve in Figure 3) more accurately captured the seasonal  
210 cycle in the daily average NEE for the three PFTs optimized in this study. The model was particularly successful in capturing  
211 the seasonal profile for the agricultural ecosystem, which can be attributed to the more pronounced seasonal transitions of sug-  
212 arcane (as indicated by the EVI), even though the low-resolution satellite indices do not fully capture the onset of the growing  
213 season. However, this allowed the model to better represent the GEE equation for this ecosystem. For the Cerrado, the model  
214 smoothed the NEE peaks, and the GEE and respiration equations were also smoothed with the optimization. Optimizing the

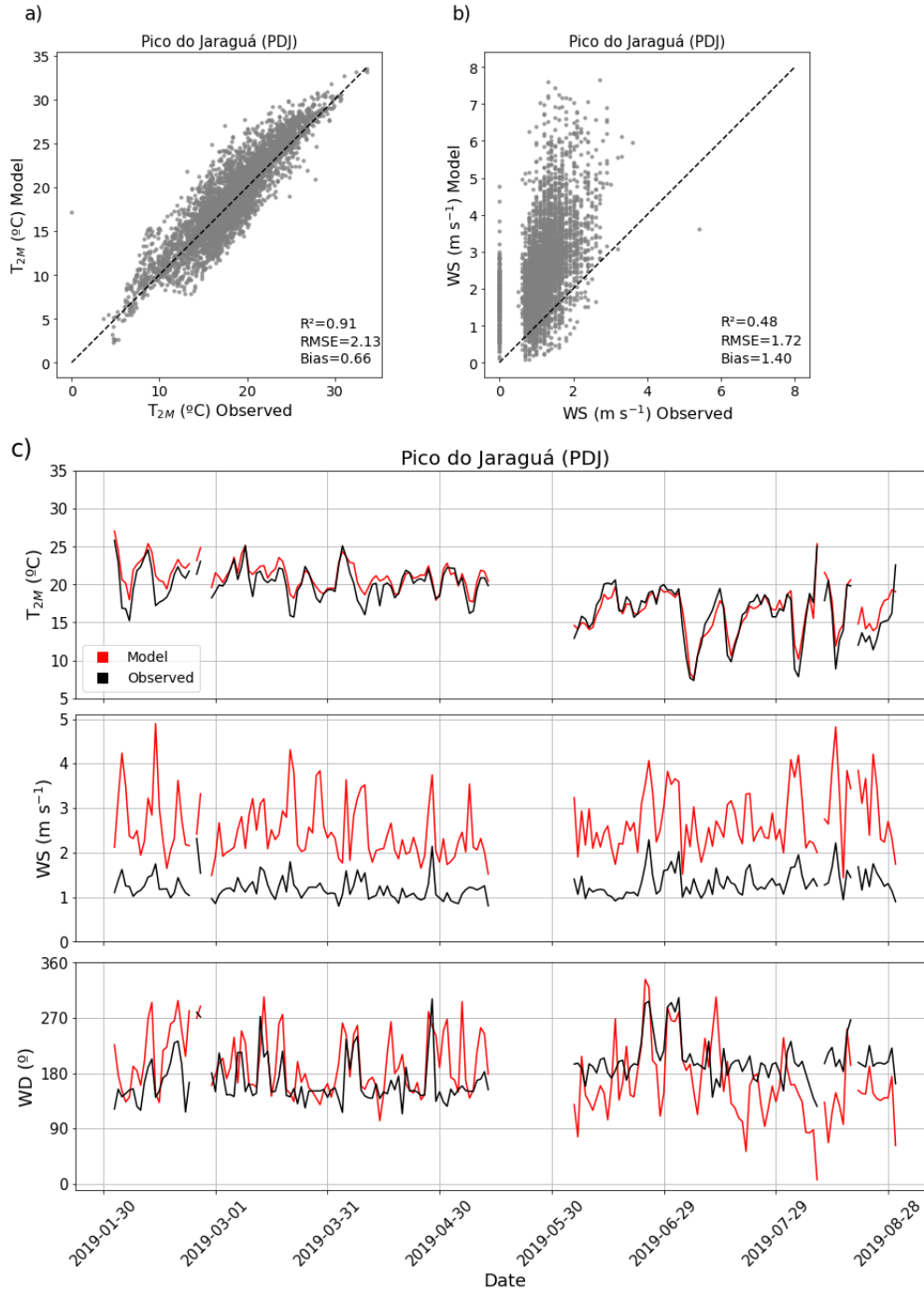


**Figure 2.** Panels (a) and (b) show scatter plots comparing model outputs and observations at the PDJ station for hourly values of 2m air temperature ( $T_{2m}$ ) and 10 m wind speed (WS), respectively. Panel (c) presents the daily averages from February to August 2019 for 2m air temperature ( $T_{2m}$ ), 10 m wind speed (WS), and wind direction (WD). The black line represents observational data, while the red line indicates model simulations.

**Table 4.** Default (Mahadevan et al., 2008) and Optimized VPRM parameters (highlighted) for Atlantic Forest, Cerrado and sugarcane, and for mixed forest and grasses from Botía et al. (2022).

Type of Vegetation (PFTs)	Default				Optimized & Botía et al. (2022)			
	PARo	$\lambda$	$\alpha$	$\beta$	PARo	$\lambda$	$\alpha$	$\beta$
<b>Atlantic Forest</b>	<b>570</b>	<b>0.127</b>	<b>0.271</b>	<b>0.250</b>	<b>178615</b>	<b>0.008</b>	<b>-0.211</b>	<b>4.715</b>
Mixed forest	629	0.123	0.244	0.240	206	0.255	0.342	0.000
Grasses	321	0.122	0.028	0.480	15475	0.056	0.312	7.337
<b>Cerrado</b>	<b>3241</b>	<b>0.057</b>	<b>0.012</b>	<b>0.580</b>	<b>2300</b>	<b>0.616</b>	<b>0.070</b>	<b>1.665</b>
<b>sugarcane</b>	<b>2051</b>	<b>0.200</b>	<b>0.209</b>	<b>0.802</b>	<b>14550</b>	<b>0.049</b>	<b>-0.339</b>	<b>10.052</b>
Urban area	0.0	0.0	0.0	0.0	0.0	0.0	0.0	0.0

VPRM parameters improved the representation of the growing season, especially for the Atlantic Forest and sugarcane, while using optimized or default parameters for the Cerrado resulted in similar NEE simulation.

The first panel in Figure 4 shows the monthly net  $CO_2$  flux simulated by the VPRM model for 2019. February represents a summer month, while August represents a winter month. The second panel shows the monthly hourly net  $CO_2$  flux simulated at the three flux tower sites used to optimize the VPRM model parameters. In February, negative NEE values are found in the northern part of the MASP, while the southern part exhibits positive NEE fluxes in the coastal region. During the summer, ecosystem productivity is expected to peak across all land cover classes, typically resulting in negative NEE. This behavior was clearly observed in February (Figure 4a) for Cerrado, sugarcane, and pasture areas. In contrast, the Atlantic Forest in the southwestern portion of the domain exhibited positive NEE values, an unexpected pattern for a summer month. This may be linked to a combination of structural and anthropogenic factors, as well as limitations of the model itself. The Atlantic Forest is marked by structural heterogeneity, extreme biodiversity, and high fragmentation, which can lead to significant local variation in  $CO_2$  fluxes. In addition, the SEEG (2021) report highlights a progressive decline in the biome’s carbon sink function. Model limitations also likely contribute to these discrepancies, particularly simplifications in VPRM’s equations of respiration and phenology, which may not fully capture the complex dynamics of ecosystems like the Atlantic Forest (Rezende et al., 2018; Segura-Barrero et al., 2025).

In August, the cold and dry conditions, due to reduced solar radiation and a lower leaf area index, resulted in positive fluxes across most of the domain and low negative fluxes in only a few areas (Figure 4b). The highest positive NEE values are found in the southern coastal region. Generally, larger areas with negative  $CO_2$  fluxes are observed in February compared to August for the same dominant land cover classes. This indicates greater  $CO_2$  absorption by agriculture in February compared to forested regions. Conversely, in August,  $CO_2$  fluxes are predominantly lower and negative across most of the domain, with higher positive values in the coastal area, especially in the south. Overall, the domain acts as a net  $CO_2$  sink during summer, while vegetation becomes a  $CO_2$  source in winter, except for the Atlantic Forest in the southern part of the study area. The second panel also shows simulated fluxes for the same flux tower sites, with negative net fluxes in February, particularly in the Atlantic Forest, sugarcane, and Cerrado. This underscores the reduction in negative fluxes during winter, as seen in the August data for

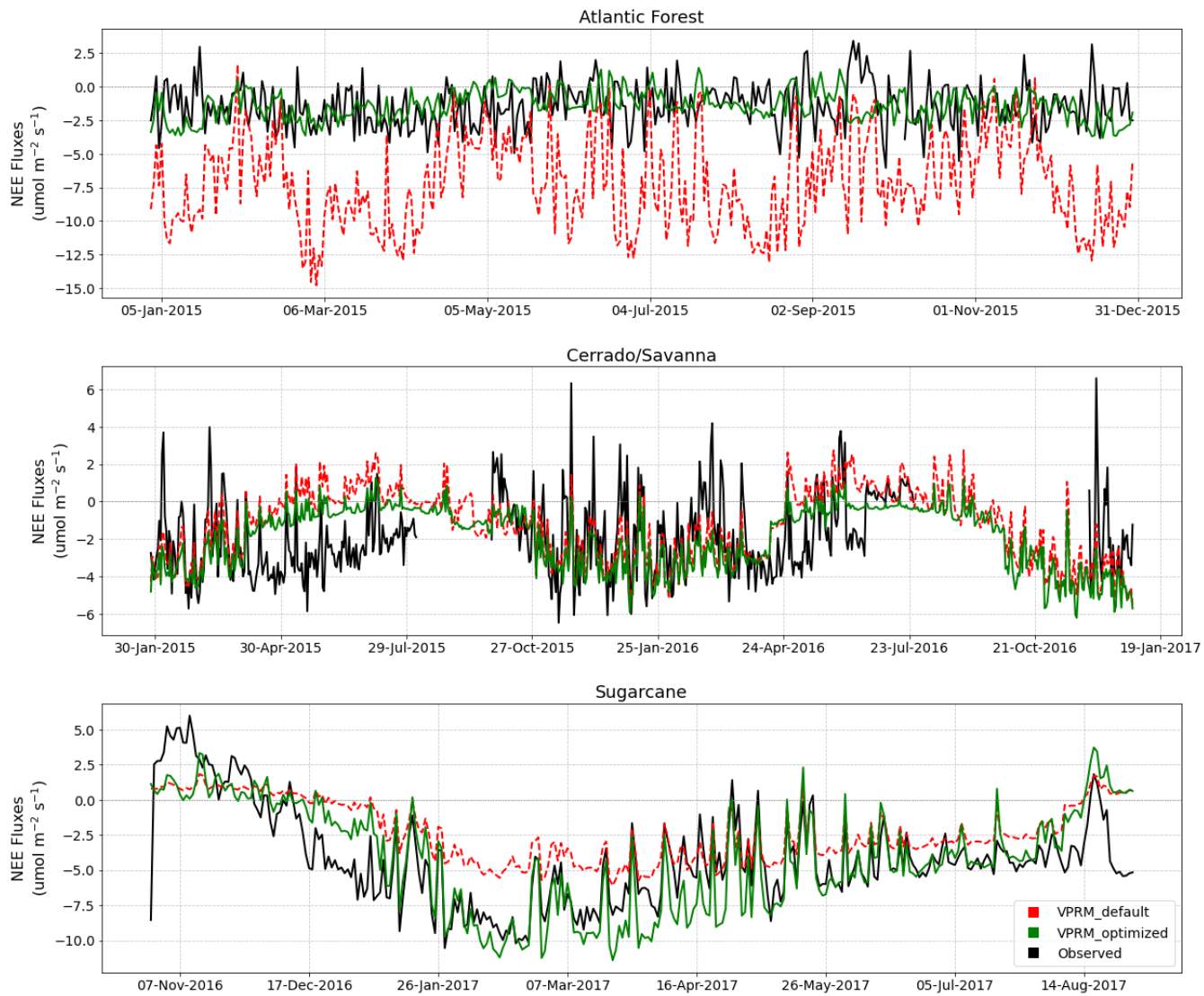


**Figure 3.** Daily variability of NEE fluxes ( $\mu\text{mol m}^{-2} \text{s}^{-1}$ ) from the flux tower (black line), compared with NEE fluxes simulated by the VPRM model using default (red line) and optimized (green line) parameters for the Atlantic Forest, Cerrado/Savanna, and sugarcane.



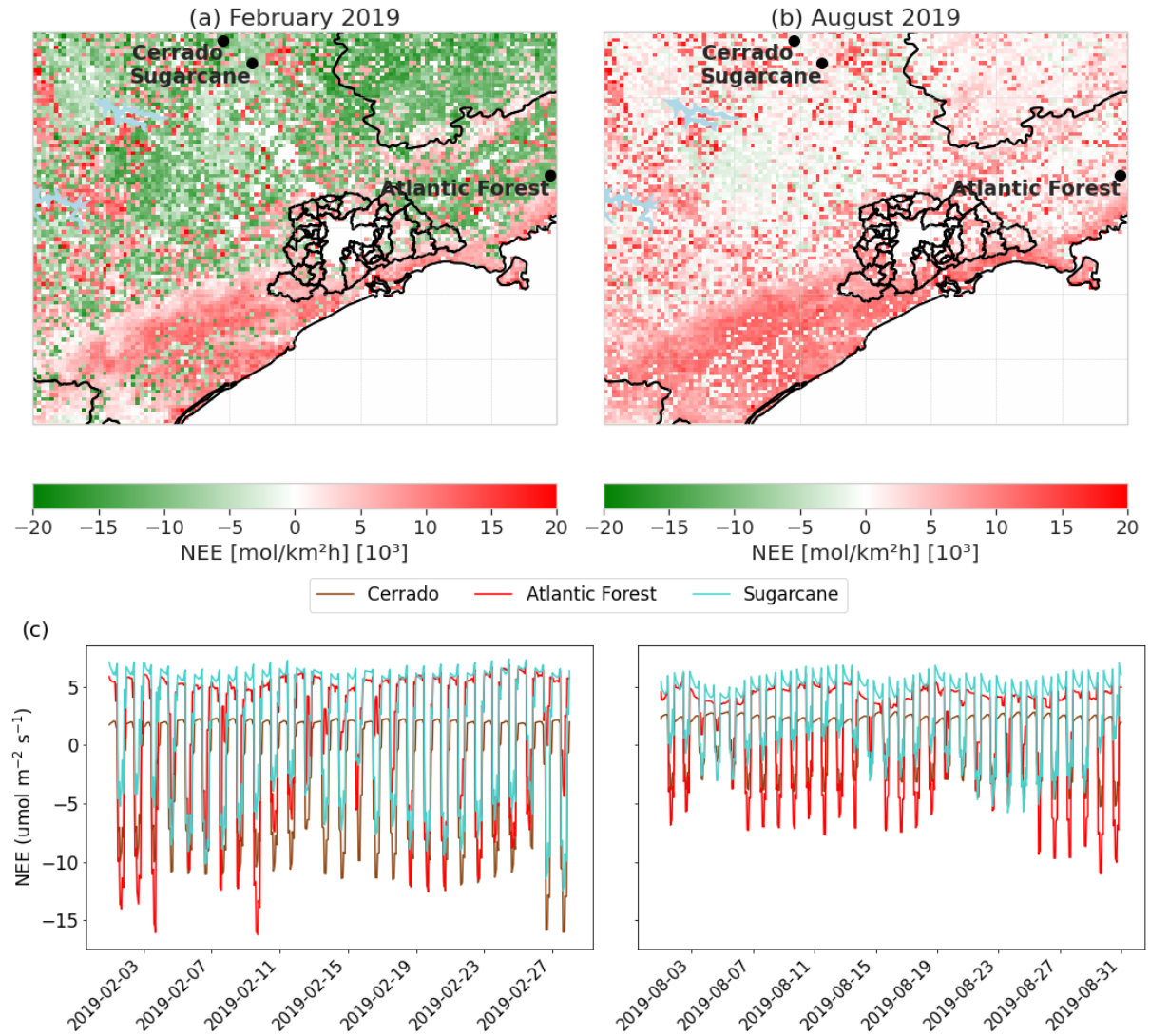


**Figure 4.** The first panel shows the monthly mean of net ecosystem exchange (NEE) ( $\text{mol km}^{-2} \text{h}^{-1}$ ) for February (a) and August (b) 2019. The second panel (c) presents the hourly variability of NEE ( $\mu\text{mol m}^{-2} \text{s}^{-1}$ ) for the same months (February and August) at three different PFTs: Atlantic Forest, Cerrado/Savanna, and sugarcane.

all three vegetation types. Unfortunately, observed data from these flux towers for this period were not available for statistical model evaluation. However, Figure 4 illustrates the significant influence of climatic drivers on reduced flux trends, consistent with findings by Raju et al. (2023) for a tropical region. Note that the respiration equation in Mahadevan et al. (2008) is a simple linear function of temperature and does not account for seasonal or spatial variability in biomass and litter inputs to soil carbon pools Gourdji et al. (2022), which is particularly relevant for forest ecosystems like the Atlantic Forest.

### 3.3 Seasonal variations in observed and modeled $CO_2$ mixing ratios

Figure 5 and Table 5 depict the monthly mean, standard deviation, bias and RMSE of  $CO_2$  concentrations at two sites in the MASP. In 2019, the IAG station recorded  $CO_2$  values ranging from 406 to 464 ppm. The seasonal variation peaked during winter (June to August,  $437.3 \pm 32.2$  ppm), followed by autumn (March to May,  $433.0 \pm 26.0$  ppm), with the lowest values observed in summer (February,  $432.7 \pm 24.6$  ppm). This variation in  $CO_2$  levels is primarily influenced by the geographical location of the observation site, as well as meteorological conditions such as wind speed and atmospheric stability, and seasonal patterns of photosynthesis and vehicular traffic (see Figure B1 in Appendix B). The maximum and minimum monthly  $CO_2$  concentrations at IAG were recorded in June ( $442.5 \pm 32.8$  ppm), during the winter season, and March ( $430.2 \pm 24.5$  ppm), during the autumn season, respectively. During this month, the MASP experiences changes in synoptic circulation and atmospheric moisture that typically reduce atmospheric stability and increase the dispersion of various gases and particles (Chiquetto et al., 2024). Meanwhile, at the PDJ station,  $CO_2$  levels ranged from 414 ppm to 417 ppm. The seasonal variation peaked during autumn ( $416.8 \pm 9.5$  ppm), closely followed by summer ( $416.0 \pm 10.3$  ppm), with the lowest values observed in winter ( $414.6 \pm 7.4$  ppm). The maximum monthly  $CO_2$  mean at PDJ was identified in May ( $417.3 \pm 9.1$  ppm), corresponding to the autumn season, while the minimum was recorded in July ( $414.0 \pm 6.3$  ppm), during the winter season. Monthly values at PDJ exhibited less variability and a smaller standard deviation compared to the IAG site. This result was expected, considering that the IAG site is significantly impacted by vehicular traffic in its vicinity. In contrast, PDJ is located at a higher elevation in a more vegetated area, with less influence from local anthropogenic sources. Additionally, lower  $CO_2$  concentrations were expected at PDJ during the summer due to the stronger vegetation signal compared to the IAG site. However, PDJ actually shows peak  $CO_2$  levels in summer and the lowest values in winter, indicating that additional ecological and ecosystem variables need to be considered for a better understanding of this location.

The simulated  $CO_2$  concentrations for the IAG station ranged from 410 ppm to 437 ppm, with a seasonal variation peaking in winter ( $429.4 \pm 19.2$  ppm), followed by autumn ( $425.2 \pm 15.1$  ppm), and the lowest values occurring in summer ( $422.3 \pm 12.3$  ppm), mirroring the observed data. Notably, the highest and lowest monthly  $CO_2$  concentrations at IAG were identified in June ( $438.7 \pm 22.5$  ppm) and February ( $418.1 \pm 10.0$  ppm), respectively. Although the maximum monthly value from the model coincided with the observed data, the month with the minimum concentration was February, which may be attributed to gaps in measurement, which were not considered when calculating the mean, thereby influencing the observed monthly mean. The  $CO_2$  concentrations at PDJ ranged from 415 ppm to 426 ppm, with seasonal variation peaking in winter ( $421.8 \pm 11.8$  ppm), followed by autumn ( $420.4 \pm 10.1$  ppm), and the lowest values occurring in summer ( $419.0 \pm 8.8$  ppm). The model data profile for PDJ more closely resembles the simulated IAG profile than the PDJ station's observed profile, which

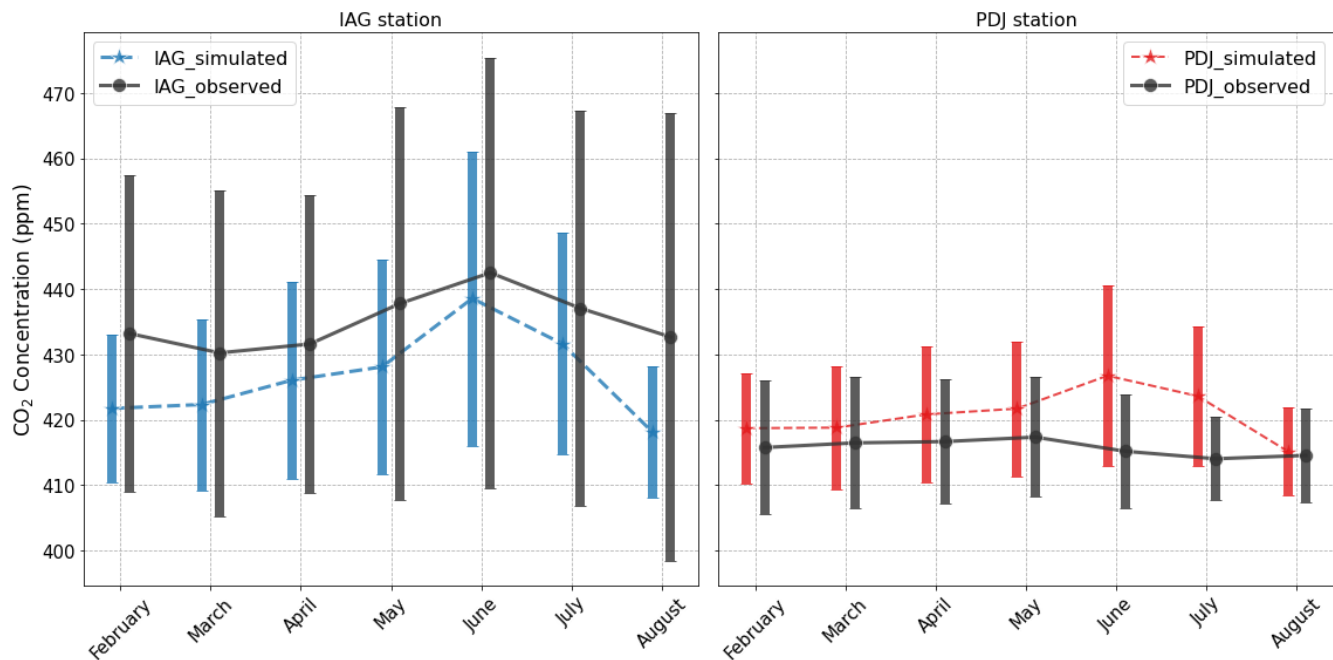


**Figure 5.**  $CO_2$  concentration seasonality observed and simulated at IAG and PDJ stations in 2019. Error bars represent the monthly standard deviation.

likely stems from model limitations, including grid resolution and insufficient representation of localized characteristics at different sites. However, negative biases were observed for all seasonal periods at IAG, indicating an underestimation of  $CO_2$  concentrations and higher RMSE compared to the statistics for the PDJ station. The PDJ station exhibited low positive biases and smaller standard deviations between the model and observations. Its higher elevation and dense vegetation cover simplify the representation of seasonal trends, reducing the influence of urban emissions and resulting in lower  $CO_2$  concentrations at this site (see Figure B7 in Appendix B).

**Table 5.** Seasonality means and standard deviation of  $CO_2$  concentrations for IAG and Pico do Jaraguá (PDJ) stations.

Station	Season	Observed (ppm)	Simulated (ppm)	Bias (ppm)	RMSE (ppm)
IAG	Summer (February)	$432.7 \pm 24.6$	$422.3 \pm 12.3$	-12.1	25.2
	Autumn (MAM)	$433.0 \pm 26.0$	$425.2 \pm 15.1$	-7.5	24.8
	Winter (JJA)	$437.3 \pm 32.2$	$429.4 \pm 19.2$	-7.2	31.1
PDJ	Summer (February)	$416.0 \pm 10.3$	$419.0 \pm 8.8$	3.6	11.1
	Autumn (MAM)	$416.8 \pm 9.5$	$420.4 \pm 10.1$	3.6	12.0
	Winter (JJA)	$414.6 \pm 7.4$	$421.8 \pm 11.8$	7.3	13.8

### 3.3.1 Distribution of surface $CO_2$ concentrations

In addition to the simulations conducted for the period from February to August 2019, using the same configurations and input data, we performed simulations involving variable emission scenarios for the summer (February) and winter (August) seasons. The aim was to comprehensively understand the dynamics of  $CO_2$  concentration in the metropolitan region and surrounding areas during these distinct seasonal periods. Figure 6 shows the monthly average spatial distributions of simulated  $CO_2$  concentrations under four conditions: a) Background without emissions, considering only boundary and initial conditions (BCK); b) considering both anthropogenic emissions and biogenic fluxes (see Table 1) (ALL); c) considering biogenic fluxes only (BIO); and d) considering anthropogenic emissions (energy, industry, residential, refinery, and vehicular sectors) only (ANT).

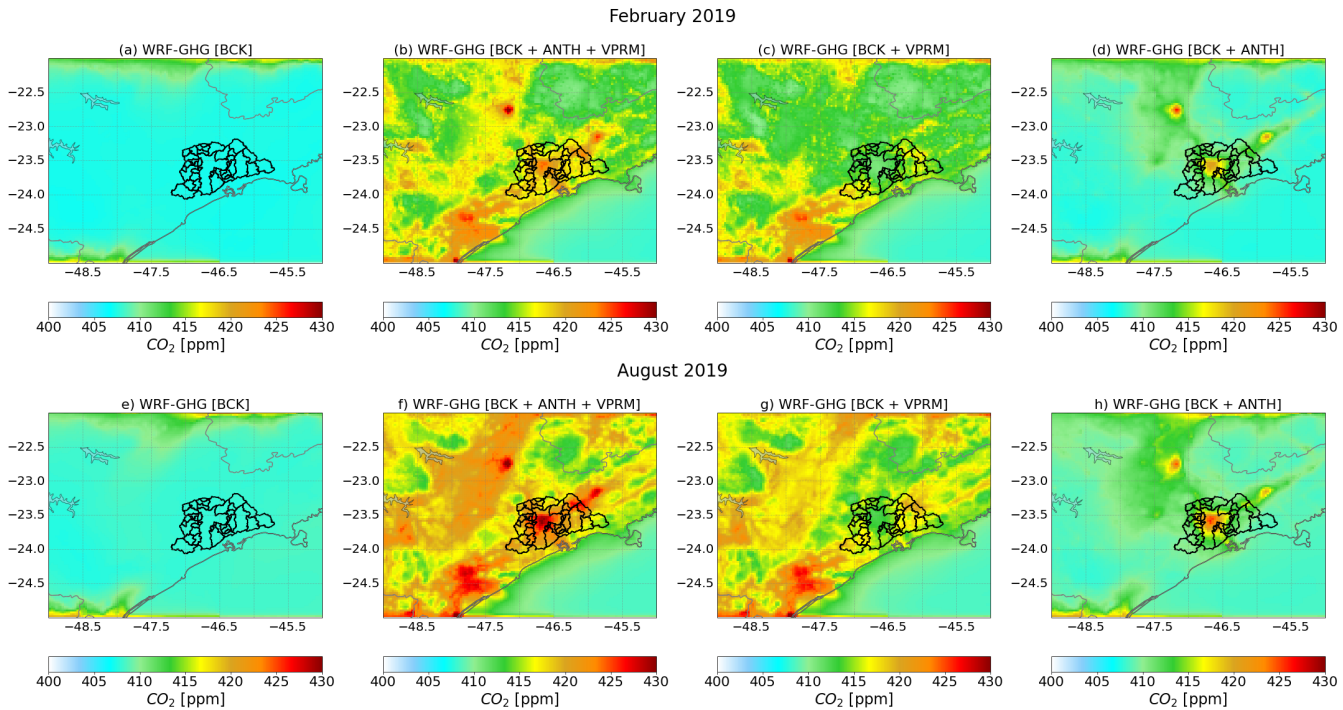


**Figure 6.** Atmospheric  $CO_2$  concentrations under different emission scenarios (refer to the text). The panels in the first row represent the monthly mean concentration for February (a, b, c, d), while the panels in the second row represent the monthly mean concentration for the August period (e, f, g, h). Panels a) and e) represent the background scenario. Panels b) and f) represent simulation of total (background, anthropogenic and biogenic) emissions scenario, panels c) and g) represent simulation of only background and biogenic scenario, and d) and h) represent simulation of only background and anthropogenic scenario.

Figure 6a shows that the simulated background  $CO_2$  concentration in February ranged around 408 ppm across most of the domain. For biogenic simulations (Figure 6c), we observed an average increase of 14 ppm across the domain compared to the previous simulation. The increase, however, was only 6 ppm in downtown MASP. Although the VPRM model did

not explicitly calculate  $CO_2$  fluxes in urban areas due to limited vegetation coverage, the transport of biogenic signals from the surrounding vegetated regions into the urban area is evident. The southwest region of the domain, characterized by the Atlantic Forest, exhibits the highest  $CO_2$  concentrations in this scenario, ranging from 420 to 424 ppm. This dense vegetation region and higher ecosystem respiration contribute to elevated  $CO_2$  levels, underscoring the influence of biogenic sources on regional concentration patterns. This region has altitudes lower than 200 m and the  $CO_2$  released to the atmosphere by the vegetation is trapped due to the Serra do Mar, with altitudes higher than 500 m. The Atlantic Forest present on the northern coast, on the other hand, is concentrated on the plateau of Serra do Mar, and thus, the  $CO_2$  released is better dispersed to other areas. The simulation with anthropogenic emissions (Figure 6d) stands out elevated  $CO_2$  concentrations over the center of the city of São Paulo, characterized by high vehicle emissions, as well as over other two urban areas in the north and northeast of MASP. The monthly mean  $CO_2$  concentration in these two urban areas was roughly 420 ppm, attributed to emissions from refineries represented by the EDGAR datasets as well as vehicles. Figure 6b shows the simulated  $CO_2$  concentration considering both vegetation fluxes and anthropogenic emissions. As expected, this simulation combines both contributions, resulting in high  $CO_2$  concentrations over urban areas and along the coastal region. For August, it can be observed that the background concentrations (Figure 6e) were slightly higher around MASP. Additionally, the monthly mean  $CO_2$  concentration for the scenario in August with only biogenic sources was 8 ppm higher than that in February, which can be explained by the lower photosynthetic rates in this period, as observed in Figure 4. The Atlantic Forest in the coastal region exhibits more positive  $CO_2$  fluxes and lower photosynthetic activities, characterized by lower amounts of rainfall in the region that contribute to this reduced photosynthetic production by vegetation. The simulation with only anthropogenic emissions (Figure 6h) shows higher  $CO_2$  concentrations compared to those in February. This increase in  $CO_2$  levels in August is attributed to a lower planetary boundary layer (PBL) height. However, it is important to point out that the EDGAR anthropogenic emission inventory generally overestimates the emissions around local anthropogenic sources (e.g., urban areas) (Seo et al., 2024). The higher simulated  $CO_2$  concentration for August compared to February, in the scenario with both biogenic and anthropogenic sources, is largely dependent on factors such as atmospheric stability and meteorological conditions. Atmospheric stability, along with meteorological variables such as humidity, solar radiation, and temperature, plays a crucial role in determining biogenic  $CO_2$  concentrations. In addition, under stable atmospheric conditions, such as those often observed during winter periods,  $CO_2$  concentrations tend to accumulate near the surface, resulting in higher concentrations, especially in urban areas. Therefore, the comparative analysis between the simulations of  $CO_2$  concentrations during summer and winter periods highlights the importance of accurately representing not only anthropogenic emissions, but also biogenic fluxes from vegetation.

### 3.3.2 Evaluation of sources contribution

In Figure 7, we applied a data selection scheme to all-time series to minimize the effects of local contributions and increase the spatial representativeness of each record, it consists of retaining daytime (09–17 h local) data, when the air is well-mixed, providing a large spatial representativeness with minimum influence from local sources (Gerbig et al., 2008; Ramonet et al., 2020). Figure 7, shows the comparison of the daily daytime average  $CO_2$  concentrations simulated by the model for February and August 2019, considering both biogenic and anthropogenic sources (see Figures 6b and 6f), at both IAG and PDJ sites.

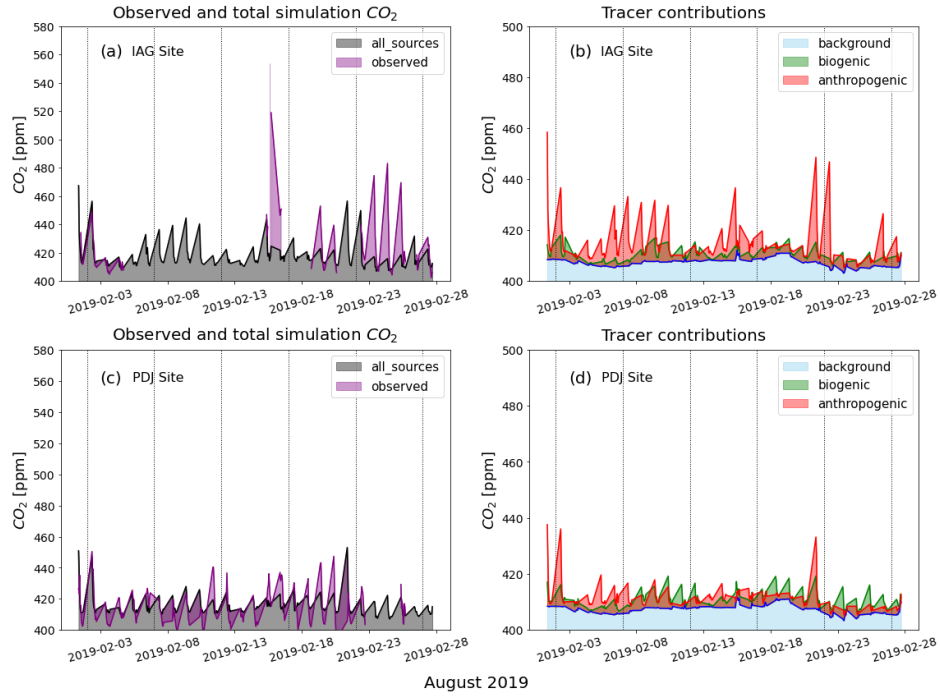
325 The left panels (Figures 7a, 7c, 7e, and 7g) depict the simulated  $CO_2$  concentration considering both anthropogenic and  
326 biogenic sources (all\_sources, in gray), alongside observed concentrations (observed, in purple) for both sites. Conversely,  
327 the right panels (Figures 7b, 7d, 7f, and 7h) display the different simulations considering anthropogenic and biogenic sources  
328 separately to the daily concentration. In Figure 7a, which represents only one summer month with available observational data  
329 (February 2019), the model generally underestimated  $CO_2$  concentrations. The observed average was 424.0 ppm, while the  
330 simulated average was 416.0 ppm an underestimation of approximately 8 ppm. This difference may be partially attributed to  
331 the presence of data gaps in the observational data for this site, as only available values were considered when calculating the  
332 monthly mean. For the anthropogenic sources the simulation is aligned with the expectations that the emission is dominated  
333 by vehicular emissions around this vicinity (Figure 7b). However, on February 23rd, 24th and 25th, there was a distinct peak  
334 in the observed  $CO_2$  concentrations. This spike is absent in both the all-source and anthropogenic simulations, suggesting that  
335 other localized or transient activities, not accounted for in the emissions inventory, may have contributed. This discrepancy  
336 likely arises because the inventories assume identical emissions for all days with only hourly variations. As a result, specific  
337 events or activities that occur on these particular days are not captured in the simulations. Furthermore, on February 2nd and  
338 22nd, observed  $CO_2$  peaks were captured by the model with similar magnitude only when both anthropogenic and biogenic  
339 emissions were included.

340 At the PDJ site, the mean observed and simulated  $CO_2$  concentration in February was 414 ppm. The model captures the  
341 overall trend and major peaks of  $CO_2$  variability during this period, with biogenic contributions more pronounced at PDJ  
342 compared to the IAG site (Figure 7d). This higher biogenic influence at PDJ is attributed to its location in a vegetated area and  
343 localized in higher altitude than IAG, relatively isolated from vehicular emissions and other anthropogenic sources typical of  
344 urban environments, as previously discussed.

345 In August, characterized by a drier, more stable boundary layer and lower wind speed, observed data for IAG showed an  
346 average of 426 ppm (Figure 7e), while with the model showed a monthly average of 413 ppm, resulting in a discrepancy of 13  
347 ppm, i.e. a higher difference compared to February. In terms of the contributions of the sources (Figure 7f), simulations showed  
348 similar daily patterns, with a few days where  $CO_2$  contributions from biogenic fluxes exceeded those from anthropogenic  
349 source. In contrast, for PDJ (Figure 7g), both the observed and simulated monthly average concentrations were 412 ppm.  
350 While the model slightly underestimated some days in the month and overestimated others, it generally captured the observed  
351 variability. Regarding the source contributions, the model simulation aligned with the observed temporal profile, displaying a  
352 more pronounced biogenic signal than at the IAG site, which further emphasizes the significant role of vegetation as a source  
353 of  $CO_2$  emissions at this location (Figure 7h). Before late August, observed values tended to be higher than the simulations,  
354 whereas in the final days of the month, the model overestimated  $CO_2$  concentrations. This overestimation is associated with  
355 an increase in background concentrations, a pattern also observed at the IAG site during the same period.

356 The bias and RMSE for each simulation at the IAG and PDJ sites for February and August 2019 are illustrated (see Figure  
357 B8 in Appendix B). At IAG, the average bias ranged from -14.31 to -9.17 ppm, while at PDJ it ranged from -3.54 to -0.96 ppm.  
358 RMSE values were consistently higher at IAG, exceeding 20 ppm in most scenarios, while PDJ showed lower errors, generally  
359 below 12 ppm.

February 2019



August 2019

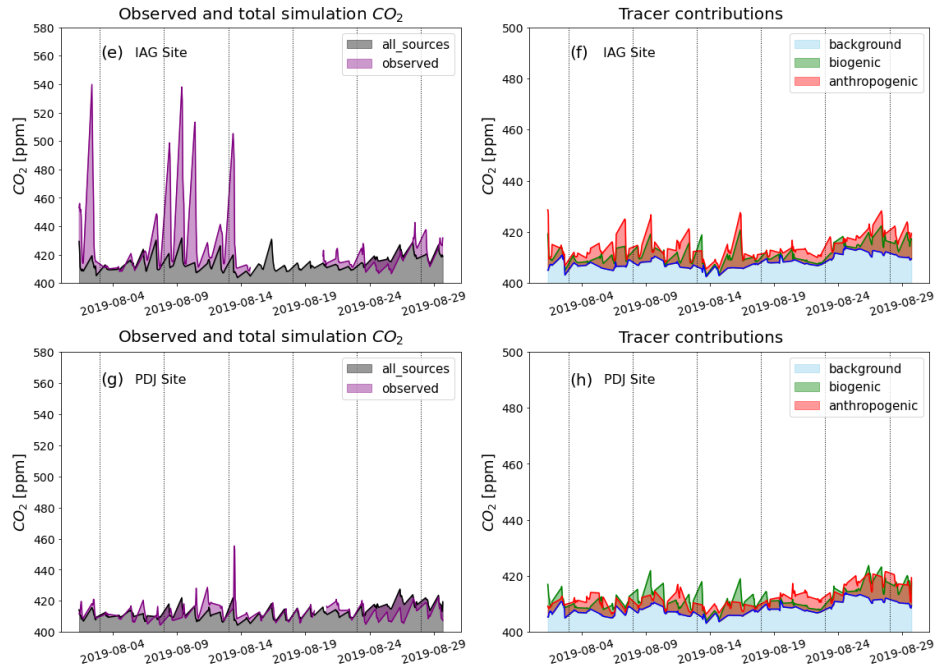


**Figure 7.** Daily mean  $CO_2$  concentrations simulated and observed for the IAG site in February 2019 (a), for the PDJ site in February (c), for the IAG site in August (e), and for the PDJ site in August (g). And the daily simulated at the BCK (background), VPRM (biogenic), and ANTH (anthropogenic) scenarios for the IAG site during February (b), for the PDJ site in February (d), for the IAG site during August (f), and for the PDJ site in August (h).

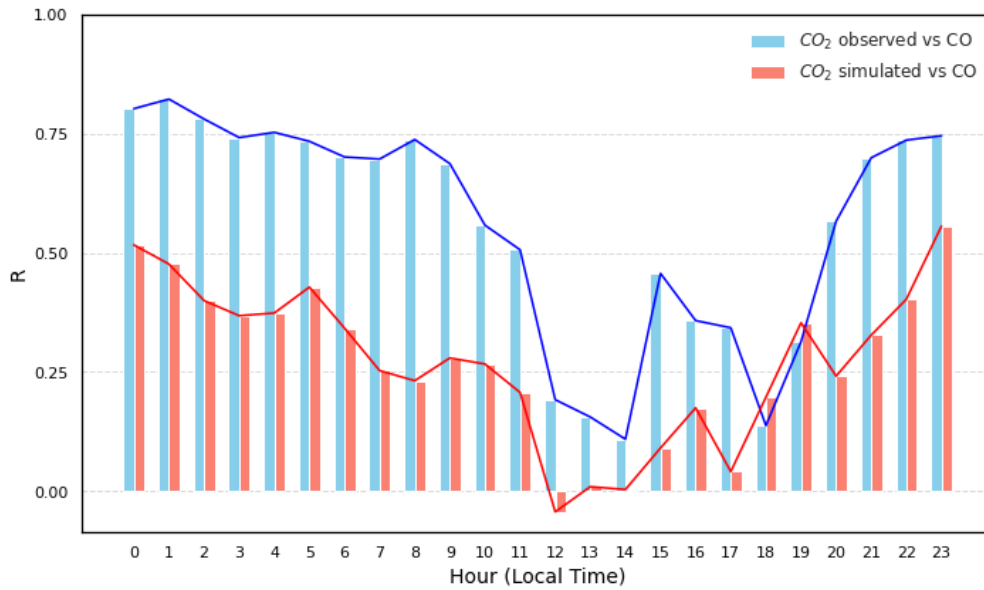


**Figure 8.** Hourly correlation between  $CO_2$  concentrations observed at the IAG site and CO concentrations observed at the Pinheiros site (blue bars), and between simulated  $CO_2$  concentrations at the IAG site and observed CO concentrations at the Pinheiros site (orange bars) for the period from February to August 2019

Considering that CO serves as a vehicular tracer, we analyzed CO concentrations at the Pinheiros site using data from the CETESB network (see Figure 1 and Table 1) to compare with  $CO_2$  concentration profiles at the IAG site for February to August 2019, located less than 3 kilometers away from the Pinheiros site. The hourly correlation between observed  $CO_2$  concentrations at the IAG site and observed CO concentrations at Pinheiros was determined, along with the correlation between simulated  $CO_2$  concentrations for IAG and observed CO concentrations. In Figure 8, both bar graphs of the hourly correlation between  $CO_2$  and CO concentrations show values above 0.5 for observed  $CO_2$  and above 0.25 for simulated  $CO_2$  during the early hours of the day (until 10h) and again in the evening (after 19h). Midday, this correlation decreases and even turns negative for the simulated  $CO_2$  vs. CO graph, suggesting the influence of the photosynthesis process on  $CO_2$  concentrations, which is also evident in the observed data. The similarity between the trend lines of the hourly correlation profiles for observed  $CO_2$  vs. CO and simulated  $CO_2$  vs. CO is evident.

In addition to the correlation between gases, Figure 9 indicates that both the modeled and observed  $CO_2$  profiles suggest that a significant portion of the  $CO_2$  concentrations at the IAG site originates from vehicular sources, as carbon monoxide is a trace gas associated with traffic emissions (Nogueira et al., 2021). Peaks in the  $CO_2$  time series at IAG are observed at the beginning, where the model fails to capture the magnitude of these concentrations. These peaks also appear in the observed CO profile at the begin of the month, confirming that a large part of the  $CO_2$  concentrations at IAG comes from vehicular sources, particularly on days with high concentrations, which are also reflected in the CO profile. However, the model struggles to simulate this high  $CO_2$  concentrations since it assumes that emissions follow the same diurnal variation every day of the



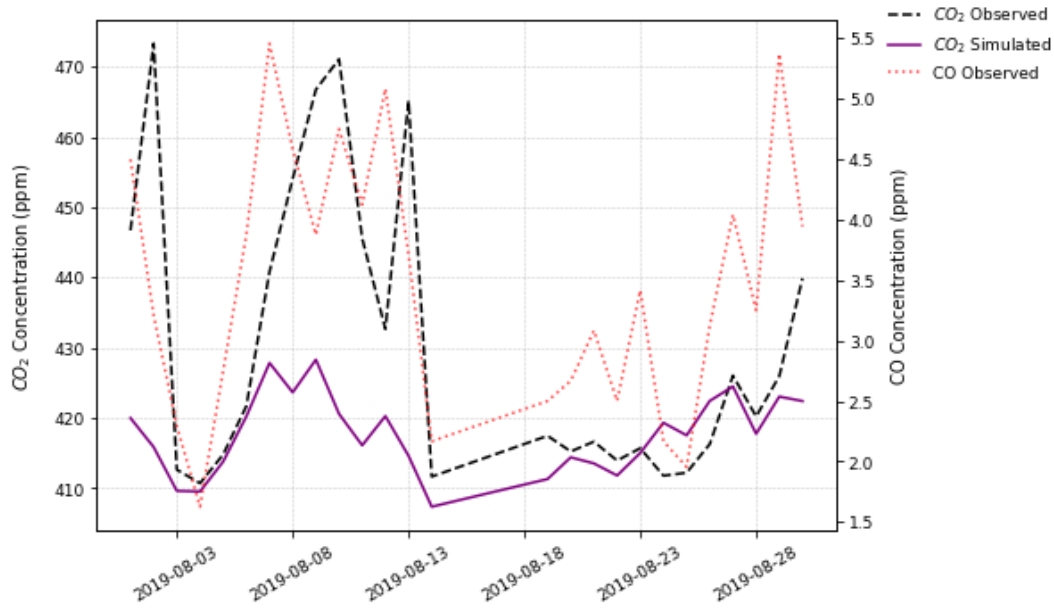


**Figure 9.** Daily mean concentrations of  $CO_2$ , both observed (black dashed line) and simulated (purple line), at the IAG site, along with observed CO concentrations (red dotted line) at the Pinheiros site during August 2019.

month. Additionally, a distinct increase in CO concentrations without a corresponding rise in  $CO_2$  was observed between August 18 and 21 and August 27 and 28, which coincided with the long-range transport of smoke plumes from Amazon forest fires to São Paulo (Bencherif et al., 2020). While biomass burning emits both CO and  $CO_2$ , their atmospheric transport and dispersion differ significantly. CO is more prevalent in incomplete combustion and tends to be transported at altitudes that favor long-range dispersion, whereas  $CO_2$  concentrations are more influenced by local emissions and atmospheric mixing (Gatti et al., 2010). These transport dynamics, combined with the long distance of the event's origin, likely explain why the CO peak was detected at Pinheiros but not accompanied by a significant  $CO_2$  enhancement at the IAG site.

### 3.3.3 Model evaluation against OCO-2 and $XCO_2$ observations

Figure 10a shows the monthly boxplots of observed and all\_sources simulated  $XCO_2$  concentrations for the period from 1 April 2019 to 31 August 2019. However, due to insufficient OCO-2 data over MASP during this period, the analysis covers all simulated domains rather than solely the metropolitan area. Regarding temporal variability, a clear seasonal cycle of  $XCO_2$  is evident from its smooth month-to-month variation (green boxes in Figure 10a). The simulated  $XCO_2$  concentrations, i.e., the simulated profiles with smoothing, generally captured this cycle, although with a less dispersion (length of the box) compared to the observed  $XCO_2$  concentrations. Notably, model-observation discrepancies are most pronounced during the winter months, with differences in median concentrations ranging from 0.8 to 1.5 ppm, while they are minimized during the autumn season,

with differences in median concentrations between 0.5 and 0.6 ppm. The simulated  $XCO_2$  concentrations demonstrate similar trends within the same range but tend to slightly underestimate values on most days.

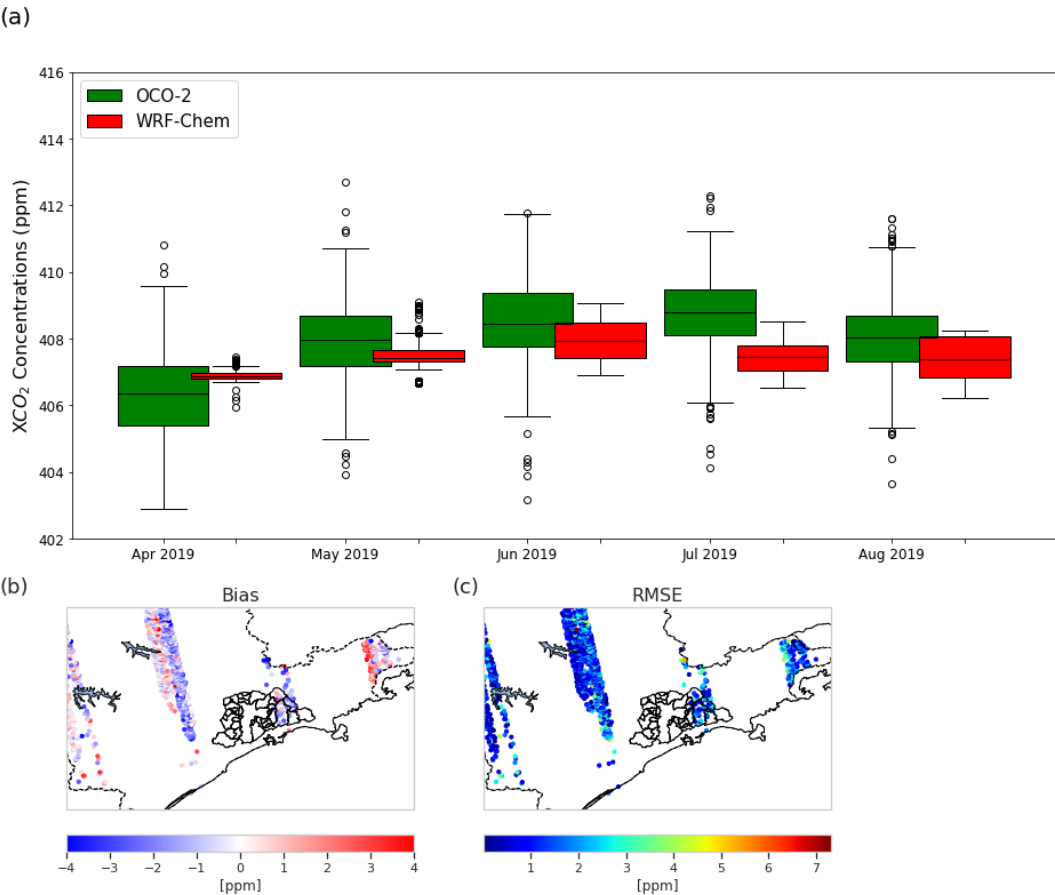


**Figure 10.** a) Monthly boxplots of observed and simulated  $XCO_2$  concentrations for the period from 1 April 2019 to 31 August 2019, b) Bias and c) RMSE calculated by pixel over the study domain.

When generating time-averaged modeled values, we only take into account the measurement period as previously mentioned. Regarding  $XCO_2$ , the smoothed column concentrations (depicted by red dotted lines in Figure B9 in Appendix B) consistently fall below the observed values on a global scale. Figure 10b and 10c depicts the bias and RMSE, respectively, calculated across the pixel-by-pixel domain. Higher RMSE values are evident in the eastern region of MASP and along the border of São Paulo and Rio de Janeiro states. In these areas, characterized by heavy vehicular traffic, the model tends to overestimate  $XCO_2$  concentrations. Conversely, for the central region of the domain, we observe slightly negative bias values accompanied by higher RMSE values, indicating an underestimation of  $XCO_2$  concentrations. The uncertainties surrounding  $XCO_2$  simulation stem from various factors, including potential biases in the model’s wind representation, particularly in urban areas, consideration of emissions solely at the surface rather than at different pressure levels, as well as errors in the initial and boundary conditions of

concentration provided by the Carbon Tracker, which has also been seen in other studies (Chen et al., 2019; Lian et al., 2021; Peiro et al., 2022).

## 4 Conclusions

A comprehensive assessment of atmospheric  $CO_2$  concentrations in the MASP and its surroundings was conducted, utilizing the WRF-Chem model using the greenhouse gas module. Given the burgeoning demand for research in this domain, particularly in South America, where urban areas are marked by significant emission sources, this study aimed to furnish a broad understanding of the key characteristics of  $CO_2$  concentrations. To ensure an accurate estimation of  $CO_2$  levels in MASP, the initial focus of the evaluation was on the model's capability to simulate meteorological variables. Biogenic fluxes were derived from the VPRM model, which was fine-tuned with flux tower data. Our results show that using this local data significantly improved simulated biogenic  $CO_2$  fluxes, highlighted the model's capacity to represent key seasonal dynamics, with negative NEE values predominating in February (summer) and positive values in August (winter). However, we recommend the deployment of additional flux towers and targeted measurement campaigns to improve the characterization other ecosystems. A more comprehensive representation of PFTs is essential, as vegetation processes play a fundamental role in shaping  $CO_2$  patterns in tropical regions. The availability of additional flux tower data would enable a more refined optimization approach, enhancing the characterization of parameters for each vegetation type. Anthropogenic emissions were curated from vehicular model and global inventory to provide a comprehensive representation of urban emissions, incorporating spatial and temporal resolution for key sources such as vehicular traffic for our domain. Boundary and initial conditions were scrutinized using global products. The WRF-Chem model demonstrated skill in simulating meteorological variables, particularly temperature; however, discrepancies in local wind speed and direction persisted. These differences are attributed to the region's complex topography and the model's resolution (3 km), which limits its ability to capture fine-scale dynamical processes.

Simulated  $CO_2$  concentrations exhibited distinct diurnal cycles influenced by local emissions, boundary layer dynamics, and vegetation fluxes. The model's performance varied between monitoring stations, highlighting the interplay between urban and vegetative environments. At the IAG site,  $CO_2$  concentrations were consistently underestimated, with negative biases of -9.17 ppm in February and -12.83 ppm in August. This underestimation was closely linked to the model's difficulty in capturing the impact of high vehicular emission densities, as indicated by the correlation with CO concentrations. Conversely, at the vegetated and elevated PDJ site, the model closely matched observational data, with minimal biases of 0.73 ppm in February and -0.61 ppm in August. In suburban locations such as the PDJ site, distant from urban sources, anthropogenic emissions diminish, and the vertical gradient of  $CO_2$  concentration generated by city emissions attenuates through atmospheric convection and diffusion processes. However, during the growing season, the contribution of biogenic flux to  $CO_2$  concentration warrants attention, especially concerning the simulation of nocturnal  $CO_2$  concentrations and ecosystem respiration. Improvements in the respiration equation of the VPRM model (Gourdji et al., 2022) could enhance the accuracy of these simulations. Importantly, the modeled  $CO_2$  concentrations exhibited high sensitivity not only to atmospheric vertical mixing near the surface but also to the prescribed temporal profiles of anthropogenic and biogenic emissions, highlighting the underestimation of ve-

436 hicular emissions. These sources of error, particularly pronounced in winter, present challenges in accurately quantifying city  
437 emissions.

438 In general, the WRF-Chem model demonstrated proficiency in simulating seasonal variations, including  $XC O_2$ , with profiles  
439 akin to OCO-2 data. This study underscores the imperative for further investigations and applications of the WRF-Chem model  
440 in uncharted regions such as the MASP, showcasing its prowess in simulating meteorological fields and  $CO_2$  observations.

441 *Code availability.* The WRF-Chem model code version 4.0 is freely distributed by NCAR at <https://www2.mmm.ucar.edu/wrf/users/download/>  
442 (Skamarock et al., 2019). The VPRM code adapted from <https://github.com/Georgy-Nerobello/VPRM-code> (Nerobello et al., 2021). VEIN  
443 can be installed from CRAN, and it is also available on Zenodo <https://doi.org/10.5281/zenodo.3714187> (Ibarra-Espinosa et al., 2018). Run  
444 control files, preprocessing and postprocessing scripts, and relevant primary input/output data sets needed to replicate the modelling results  
445 are available upon request from the corresponding author.

446 *Data availability.* All datasets and model results corresponding to this study are available upon request from the corresponding author.

447 *Author contributions.* RA performed the simulations and prepared the manuscript with the support of all co-authors. RA and RY design the  
448 experiment. TL and RB provided support to set up and run VPRM parameters optimization. OC, MM, and HR provided the observed data  
449 used in this work. RA, RY, TL, RB, AV, MA, NR, and CK contributed to the analysis and interpretation of the results.

450 *Competing interests.* The authors declare that they have no conflict of interest.

451 *Acknowledgements.* This work was supported by the National Council for Scientific and Technological Development (CNPq) fellowship  
452 process number 141962/2019-4, the FAPESP (process number 2016/18438-0 and 2021/11762-5), the French Ministry of Research (Junior  
453 Chair professor CASAL) and the Innovation Fund Denmark through the INNO-CCUS project MONICA, the National Institute of Science  
454 and Technology – INCT Klimapolis, which is funded by the Brazilian Ministry of Science, Technology, and Innovation (MCTI), and the  
455 National Council for Scientific and Technological Development (CNPq) under project number 406728/2022-4.

## 456 **Appendix A: Metrics evaluation**

$$457 \text{ Bias} = \frac{\sum_{i=1}^N (\text{pred}_i - \text{obs}_i)}{N} \quad (\text{A1})$$

$$RMSE = \sqrt{\frac{\sum_{i=1}^N (pred_i - obs_i)^2}{N}} \quad (A2)$$

$$R^2 = \frac{\sum_{i=1}^N (pred_i - \overline{pred_i})(obs_i - \overline{obs_i})}{\sqrt{\sum_{i=1}^N (pred_i - \overline{pred_i})^2 \sum_{i=1}^N (obs_i - \overline{obs_i})^2}} \quad (A3)$$

where  $pred_i$  is the model simulation value,  $obs_i$  is the observed value, and  $N$  is the number of observations.

## Appendix B: Supplementary figures

This appendix contains figures that give some additional insight to the conclusions given in the sections above and are referenced in the text.

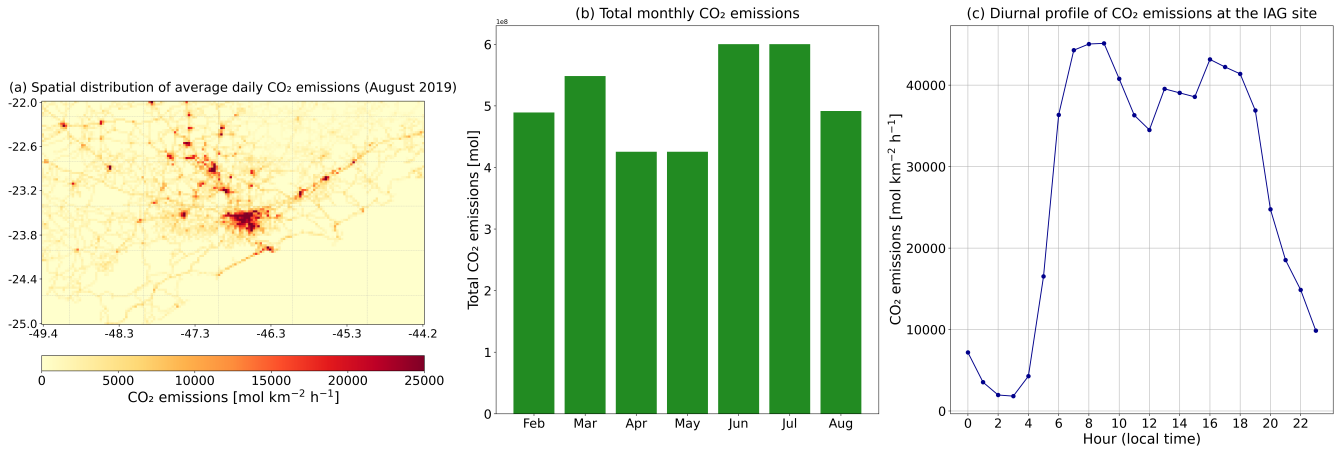


**Figure B1.** Vehicular  $CO_2$  emissions as estimated by the VEIN model over the study domain (D01). The panel (a) represents the spatial distribution of average daily  $CO_2$  emissions for August 2019 over D01. Panel (b) represents the total monthly  $CO_2$  emissions from February to August 2019 over the D01. Panel (c) shows the diurnal profile of  $CO_2$  emissions at the IAG site during August 2019.

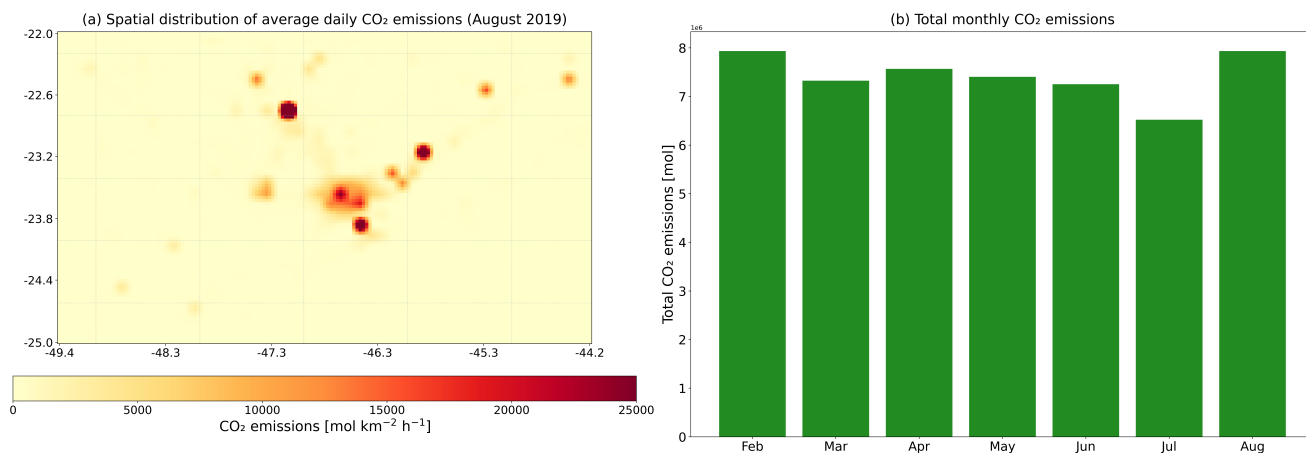


**Figure B2.** CO<sub>2</sub> emissions from energy, residential, refineries, and industry sectors by the EDGAR inventory over the study domain (D01). Panel (a) shows the spatial distribution of average daily CO<sub>2</sub> emissions for August 2019 over D01. The panel (b) represents the monthly total CO<sub>2</sub> emissions from February to August 2019 over the domain.

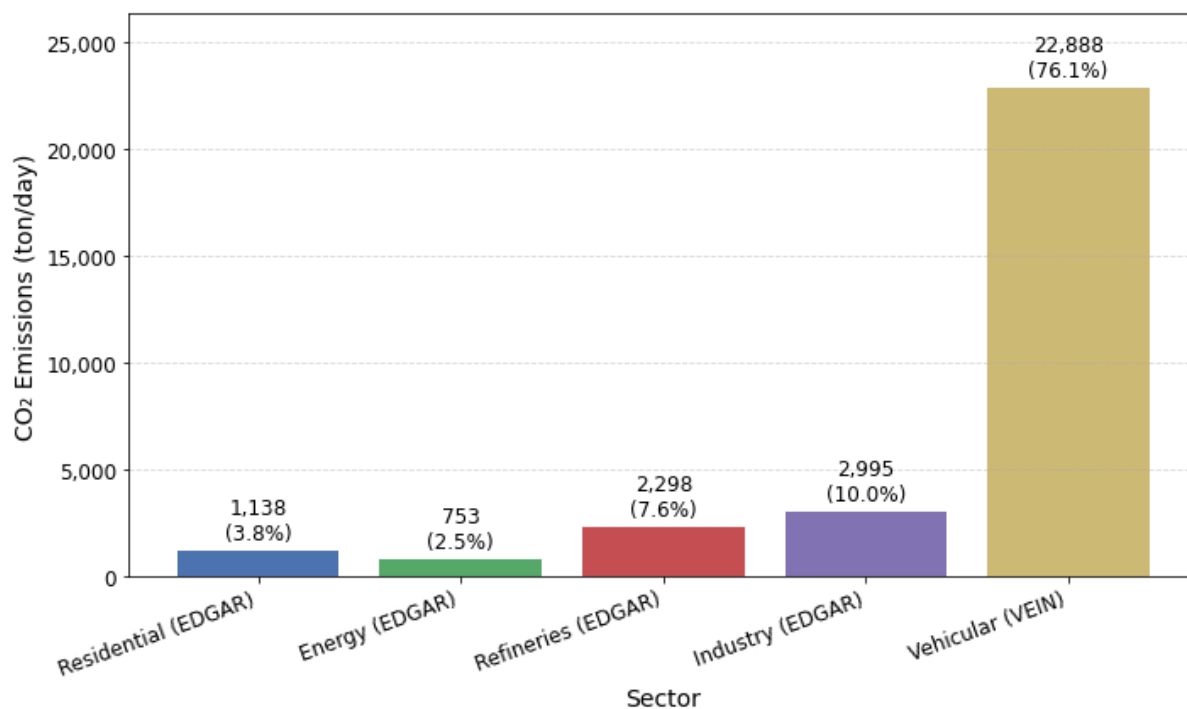


**Figure B3.** Average daily anthropogenic CO<sub>2</sub> emissions (in tons) for August 2019 within the simulated domain, disaggregated by sector. Bars represent the mean daily emissions per sector, while percentages indicate each sector's relative contribution to total anthropogenic emissions

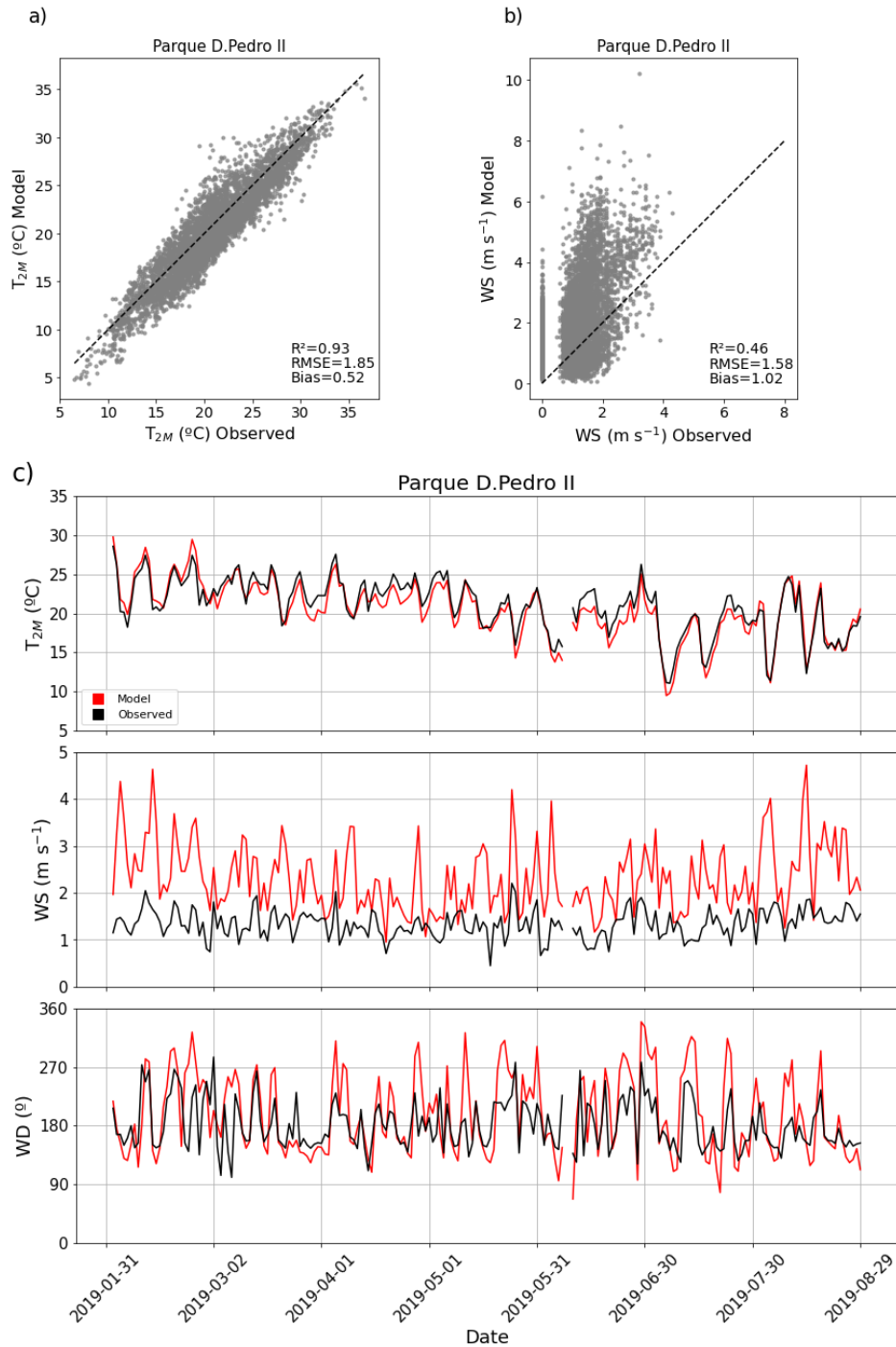


**Figure B4.** Panels (a) and (b) show scatter plots comparing model outputs and observations at the Parque D. Pedro II station for hourly values of 2m air temperature ( $T_{2m}$ ) and 10 m wind speed (WS), respectively. Panel (c) presents the daily averages from February to August 2019 for 2m air temperature ( $T_{2m}$ ), 10 m wind speed (WS), and wind direction (WD). The black line represents observational data, while the red line indicates model simulations.

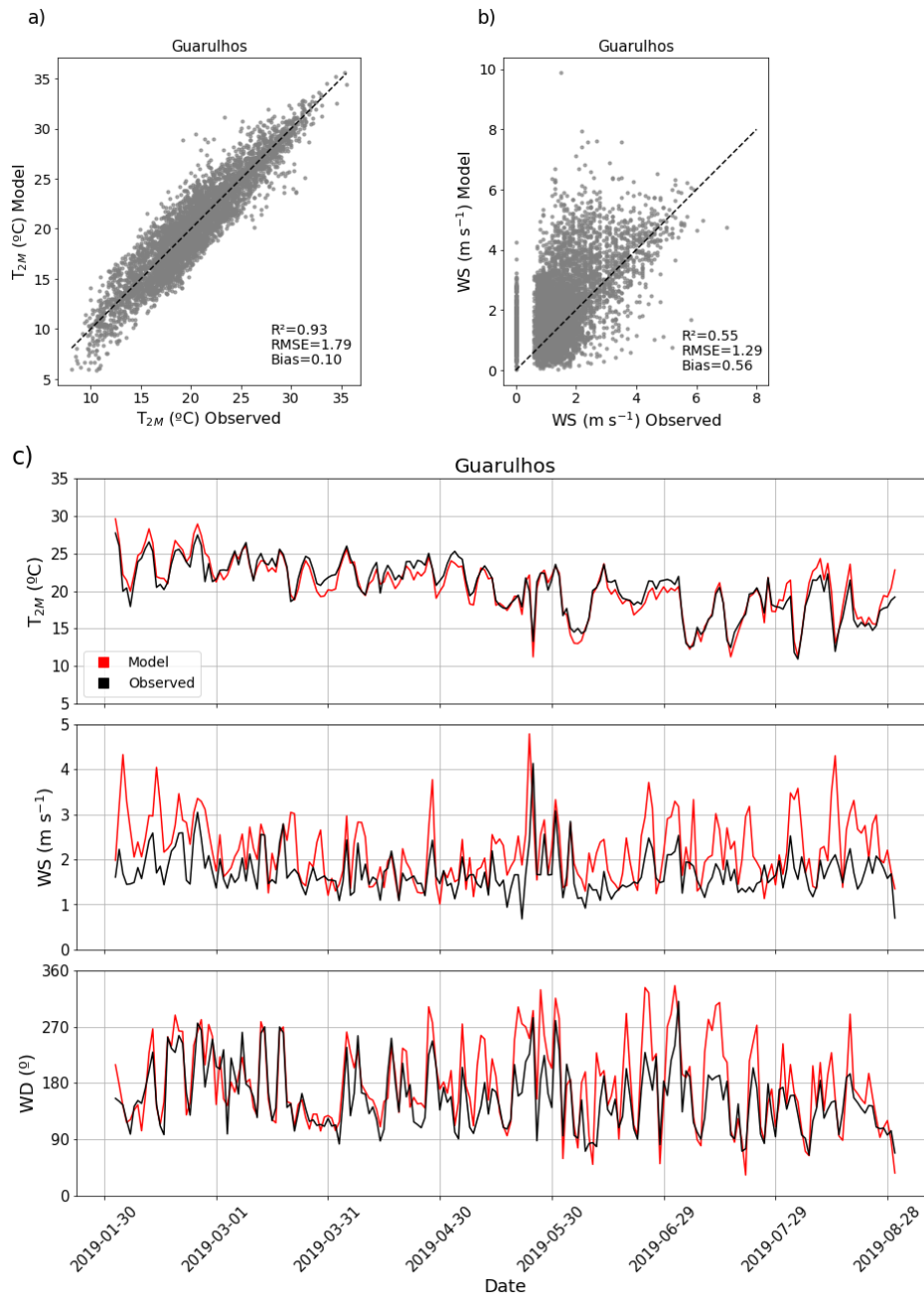


**Figure B5.** Panels (a) and (b) show scatter plots comparing model outputs and observations at the Guarulhos station for hourly values of 2m air temperature ( $T_{2m}$ ) and 10 m wind speed (WS), respectively. Panel (c) presents the daily averages from February to August 2019 for 2m air temperature ( $T_{2m}$ ), 10 m wind speed (WS), and wind direction (WD). The black line represents observational data, while the red line indicates model simulations.



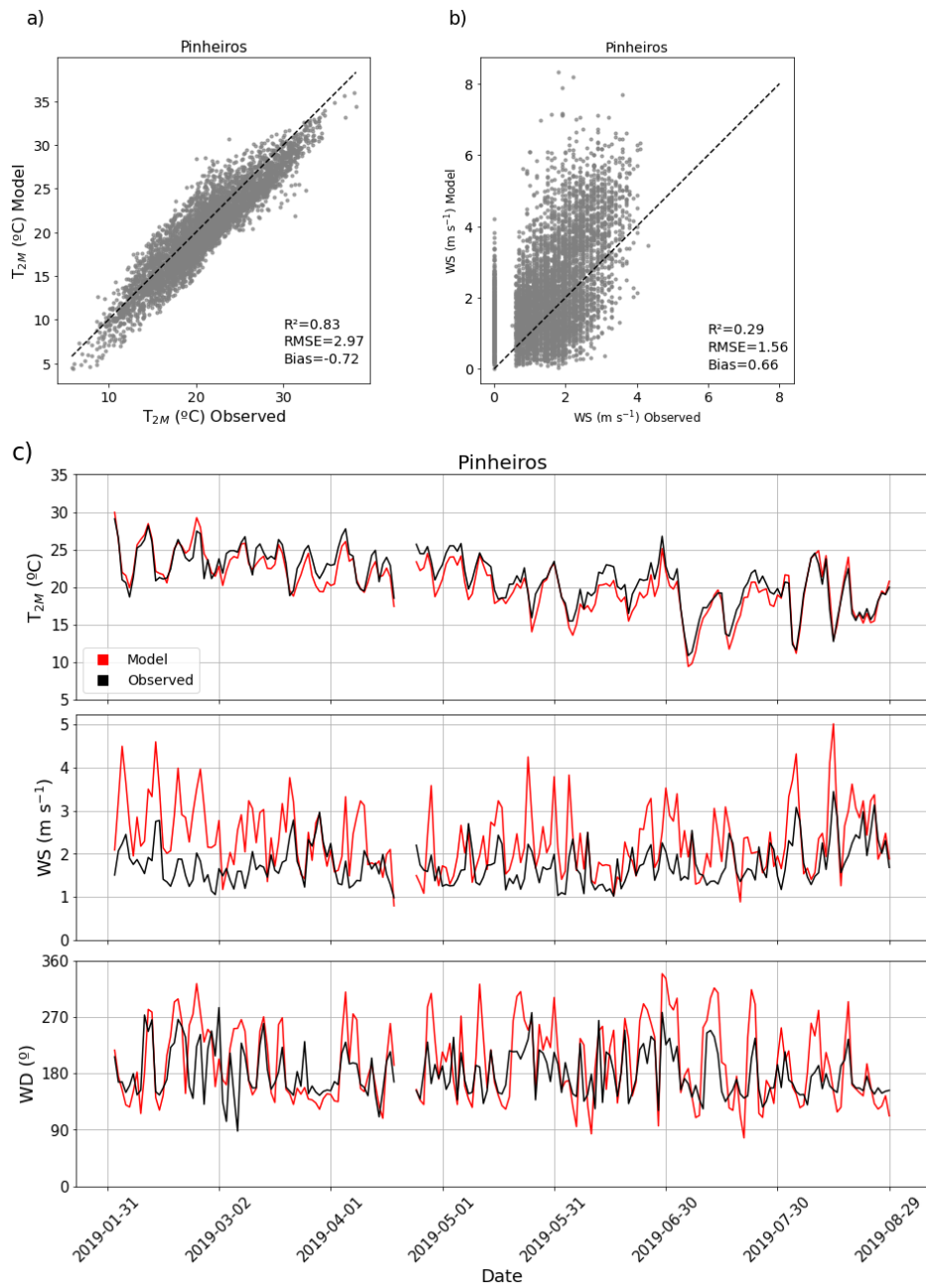


**Figure B6.** Panels (a) and (b) show scatter plots comparing model outputs and observations at the Pinheiros station for hourly values of 2m air temperature ( $T_{2m}$ ) and 10 m wind speed (WS), respectively. Panel (c) presents the daily averages from February to August 2019 for 2m air temperature ( $T_{2m}$ ), 10 m wind speed (WS), and wind direction (WD). The black line represents observational data, while the red line indicates model simulations.

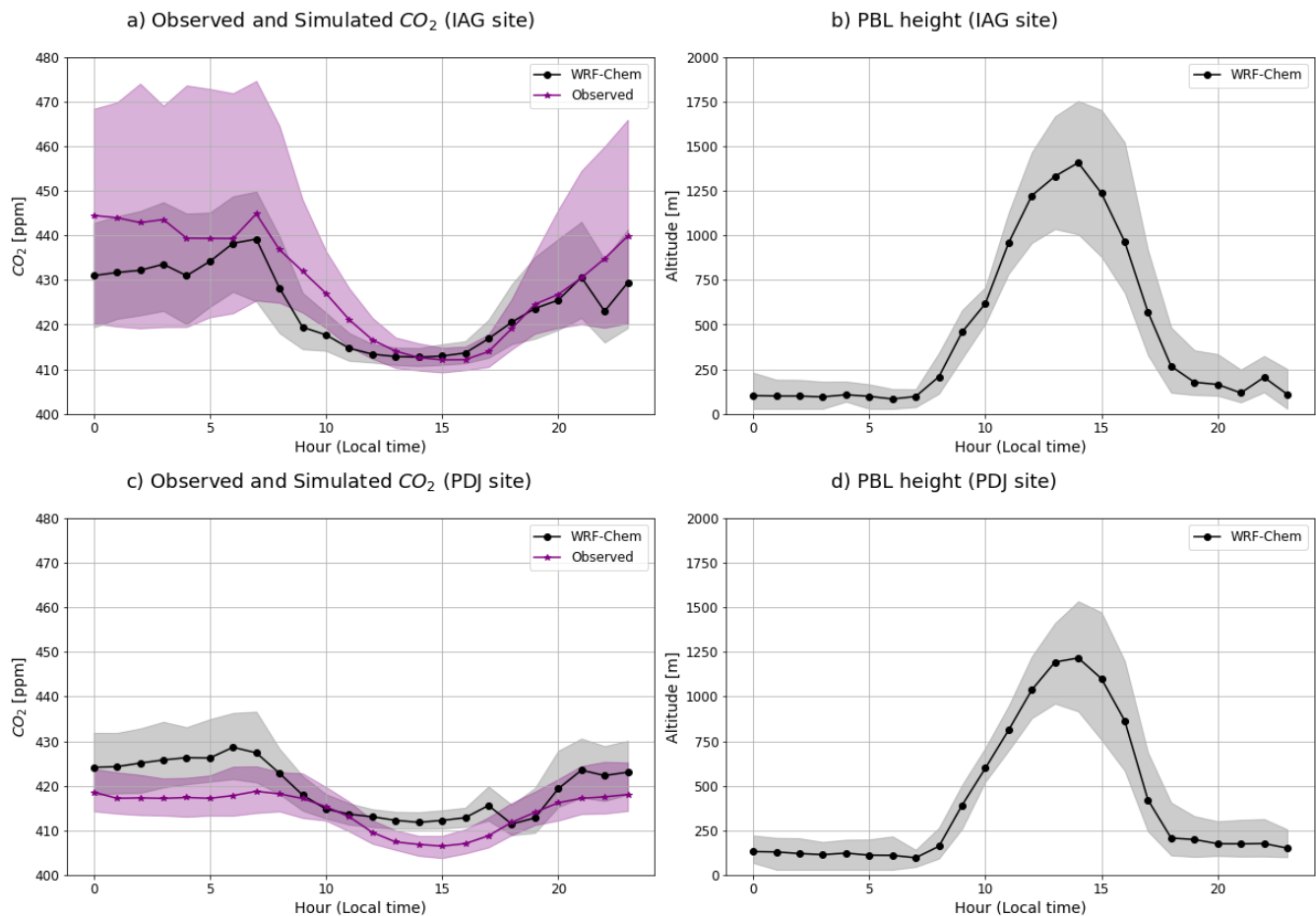


**Figure B7.** Diurnal cycle of in situ  $CO_2$  concentration and planetary boundary layer (PBL) height for the entire simulated period. The black line represents the median hourly concentrations from WRF-Chem, while the purple line corresponds to the observed values. The shaded areas indicate the interquartile ranges. Panel a) shows the observed and simulated surface  $CO_2$  concentration at the IAG site; b) the simulated PBL height at the IAG site; c) the observed and simulated surface  $CO_2$  concentration at the PDJ site; and d) the simulated PBL height at the PDJ site.

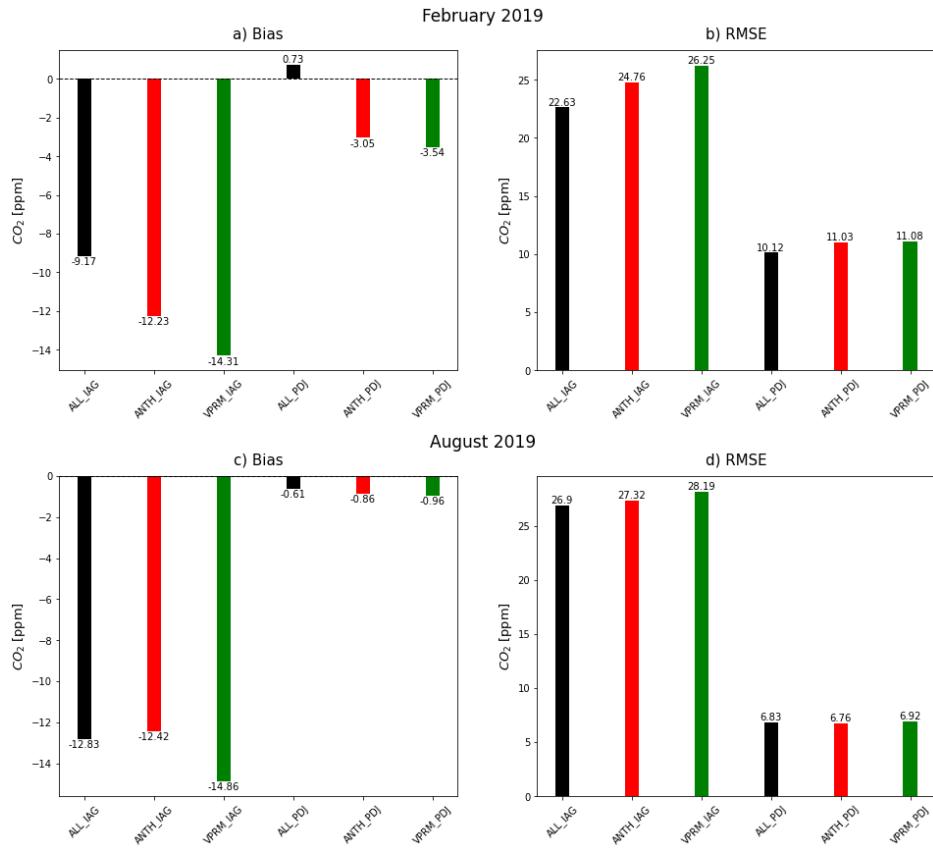


**Figure B8.** Bias (ppm) and RMSE (ppm) for each simulation at the surface  $CO_2$  observation sites. Panels (a) and (b) represent the simulations for February, while panels (c) and (d) represent the simulations for August (ALL\_\*: black, ANTH\_\*: red, VPRM\_\*: green) \*Represents the observation sites, e.g. IAG and PDJ.

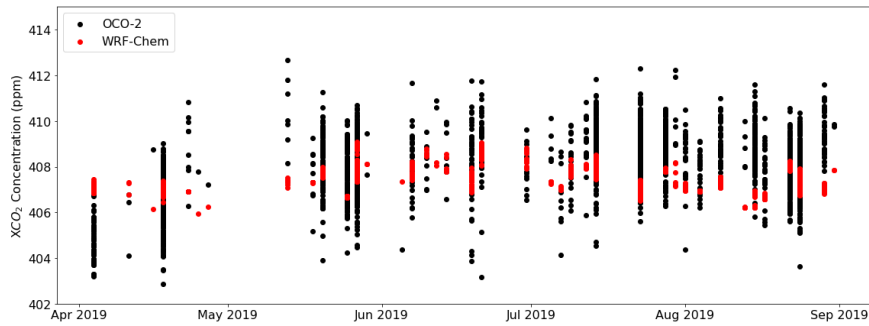


**Figure B9.** Time series of smoothed column concentrations observed (black) and modeled (red) for the period from 1 April 2019 to 31 August 2019.

## 464 References

- 465 Andrade, M. d. F., Ynoue, R. Y., Freitas, E. D., Todesco, E., Vara Vela, A., Ibarra, S., Martins, L. D., Martins, J. A., and Carvalho, V. S. B.:  
466 Air quality forecasting system for Southeastern Brazil, *Frontiers in environmental Science*, 3, 9, 2015.
- 467 Benavente, N. R., Vara-Vela, A. L., Nascimento, J. P., Acuna, J. R., Damascena, A. S., de Fatima Andrade, M., and Yamasoe, M. A.: Air  
468 quality simulation with WRF-Chem over southeastern Brazil, part I: Model description and evaluation using ground-based and satellite  
469 data, *Urban Climate*, 52, 101 703, 2023.
- 470 Bencherif, H., Bègue, N., Kirsch Pinheiro, D., Du Preez, D. J., Cadet, J.-M., da Silva Lopes, F. J., Shikwambana, L., Landulfo, E., Vescovini,  
471 T., Labuschagne, C., et al.: Investigating the long-range transport of aerosol plumes following the Amazon fires (August 2019): a multi-  
472 instrumental approach from ground-based and satellite observations, *Remote Sensing*, 12, 3846, 2020.
- 473 Botía, S., Komiya, S., Marshall, J., Koch, T., Gałkowski, M., Lavric, J., Gomes-Alves, E., Walter, D., Fisch, G., Pinho, D. M., et al.: The CO<sub>2</sub>  
474 record at the Amazon Tall Tower Observatory: A new opportunity to study processes on seasonal and inter-annual scales, *Global Change*  
475 *Biology*, 28, 588–611, 2022.
- 476 Cabral, O. M., Freitas, H. C., Cuadra, S. V., de Andrade, C. A., Ramos, N. P., Grutzmacher, P., Galdos, M., Packer, A. P. C., da Rocha,  
477 H. R., and Rossi, P.: The sustainability of a sugarcane plantation in Brazil assessed by the eddy covariance fluxes of greenhouse gases,  
478 *Agricultural and Forest Meteorology*, 282, 107 864, 2020.
- 479 Caetano, P. M. D., Pereira, H. M. S. B., Figueiredo, L. C. R., Sepe, P. M., and Giatti, L. L.: The City of São Paulo’s Environmental Quota:  
480 A Policy to Embrace Urban Environmental Services and Green Infrastructure Inequalities in the Global South, *Frontiers in Sustainable*  
481 *Cities*, 3, 685 875, 2021.
- 482 CETESB: Relatório de Qualidade do Ar no Estado de São Paulo, Tech. rep., CETESB, São Paulo, Brasil, 2019.
- 483 Change, I. C. et al.: Impacts, adaptation and vulnerability, Part A: global and sectoral aspects. Contribution of working group II to the fifth  
484 assessment report of the intergovernmental Panel on Climate Change, 1132, 2014.
- 485 Che, K., Cai, Z., Liu, Y., Wu, L., Yang, D., Chen, Y., Meng, X., Zhou, M., Wang, J., Yao, L., et al.: Lagrangian inversion of anthropogenic  
486 CO<sub>2</sub> emissions from Beijing using differential column measurements, *Environmental Research Letters*, 17, 075 001, 2022.
- 487 Chen, H. W., Zhang, F., Lauvaux, T., Davis, K. J., Feng, S., Butler, M. P., and Alley, R. B.: Characterization of regional-scale CO<sub>2</sub> transport  
488 uncertainties in an ensemble with flow-dependent transport errors, *Geophysical Research Letters*, 46, 4049–4058, 2019.
- 489 Chiquetto, J. B., Machado, P. G., Mouette, D., and Ribeiro, F. N. D.: Air quality improvements from a transport modal change in the São  
490 Paulo megacity, *Science of The Total Environment*, 945, 173 968, 2024.
- 491 Connor, B. J., Boesch, H., Toon, G., Sen, B., Miller, C., and Crisp, D.: Orbiting Carbon Observatory: Inverse method and prospective error  
492 analysis, *Journal of Geophysical Research: Atmospheres*, 113, 2008.
- 493 Crippa, M., Guizzardi, D., Muntean, M., Schaaf, E., Lo Vullo, E., Solazzo, E., Monforti-Ferrario, F., Olivier, J., and Vignati, E.: EDGAR v6.  
494 0 greenhouse gas emissions. European Commission, Joint Research Centre (JRC), 2021.
- 495 Crisp, D.: Measuring atmospheric carbon dioxide from space with the Orbiting Carbon Observatory-2 (OCO-2), in: *Earth observing systems*  
496 xx, vol. 9607, p. 960702, SPIE, 2015.
- 497 De Pue, J., Wieneke, S., Bastos, A., Barrios, J. M., Liu, L., Ciais, P., Arboleda, A., Hamdi, R., Maleki, M., Maignan, F., et al.: Temporal  
498 variability of observed and simulated gross primary productivity, modulated by vegetation state and hydrometeorological drivers, *Biogeo-*  
499 *sciences*, 20, 4795–4818, 2023.

500 Deng, A., Lauvaux, T., Davis, K. J., Gaudet, B. J., Miles, N., Richardson, S. J., Wu, K., Sarmiento, D. P., Hardesty, R. M., Bonin, T. A., et al.:  
501 Toward reduced transport errors in a high resolution urban CO<sub>2</sub> inversion system, *Elem Sci Anth*, 5, 20, 2017.

502 Feng, S., Lauvaux, T., Newman, S., Rao, P., Ahmadov, R., Deng, A., Díaz-Isaac, L. I., Duren, R. M., Fischer, M. L., Gerbig, C., et al.: Los  
503 Angeles megacity: a high-resolution land–atmosphere modelling system for urban CO<sub>2</sub> emissions, *Atmospheric Chemistry and Physics*,  
504 16, 9019–9045, 2016.

505 Freitas, H. C. d.: A influência dos transportes advectivos na estimativa do balanço de CO<sub>2</sub> do ecossistema: Um estudo de caso para a mata  
506 atlântica com uso de técnicas micrometeorológicas, Ph.D. thesis, Universidade de São Paulo, 2012.

507 Gatti, L. V., Miller, J., D’amelio, M. a., Martinewski, A., Basso, L., Gloor, M., Wofsy, S., and Tans, P.: Vertical profiles of CO<sub>2</sub> above eastern  
508 Amazonia suggest a net carbon flux to the atmosphere and balanced biosphere between 2000 and 2009, *Tellus B: Chemical and Physical*  
509 *Meteorology*, 62, 581–594, 2010.

510 Gavidia-Calderón, M., Schuch, D., Vara-Vela, A., Inoue, R., Freitas, E. D., Albuquerque, T. T. d. A., Zhang, Y., de Fatima Andrade, M., and  
511 Bell, M. L.: Air quality modeling in the metropolitan area of São Paulo, Brazil: A review, *Atmospheric Environment*, p. 120301, 2023.

512 Gerbig, C., Körner, S., and Lin, J.: Vertical mixing in atmospheric tracer transport models: error characterization and propagation, *Atmo-  
513 spheric Chemistry and Physics*, 8, 591–602, 2008.

514 Gourdji, S. M., Karion, A., Lopez-Coto, I., Ghosh, S., Mueller, K. L., Zhou, Y., Williams, C. A., Baker, I. T., Haynes, K. D., and Whetstone,  
515 J. R.: A modified Vegetation Photosynthesis and Respiration Model (VPRM) for the eastern USA and Canada, evaluated with comparison  
516 to atmospheric observations and other biospheric models, *Journal of Geophysical Research: Biogeosciences*, 127, e2021JG006 290, 2022.

517 He, J., Li, W., Zhao, Z., Zhu, L., Du, X., Xu, Y., Sun, M., Zhou, J., Ciais, P., Wigneron, J.-P., et al.: Recent advances and challenges in  
518 monitoring and modeling of disturbances in tropical moist forests, *Frontiers in Remote Sensing*, 5, 1332 728, 2024.

519 Hersbach, H.: ERA5 reanalysis is in production, *ECMWF newsletter*, 147, 5, 2016.

520 Hong, S.-Y., Noh, Y., and Dudhia, J.: A new vertical diffusion package with an explicit treatment of entrainment processes, *Monthly weather  
521 review*, 134, 2318–2341, 2006.

522 Iacono, M. J., Delamere, J. S., Mlawer, E. J., Shephard, M. W., Clough, S. A., and Collins, W. D.: Radiative forcing by long-lived greenhouse  
523 gases: Calculations with the AER radiative transfer models, *Journal of Geophysical Research: Atmospheres*, 113, 2008.

524 Ibarra-Espinosa, S., Ynoue, R., O’Sullivan, S., Pebesma, E., Andrade, M. d. F., and Osses, M.: VEIN v0. 2.2: an R package for bottom–up  
525 vehicular emissions inventories, *Geoscientific Model Development*, 11, 2209–2229, 2018.

526 IBGE: Instituto Brasileiro de Geografia e Estatística (IBGE), 2021.

527 Kaiser, W., Zhuravlev, R., Ganshin, A., Valsala, V. K., Andrews, A., Chmura, L., Dlugokencky, E., Haszpra, L., Langenfelds, R. L.,  
528 Machida, T., et al.: A high-resolution inverse modelling technique for estimating surface CO<sub>2</sub> fluxes based on the NIES-TM-FLEXPART  
529 coupled transport model and its adjoint.

530 Lian, J., Bréon, F.-M., Broquet, G., Lauvaux, T., Zheng, B., Ramonet, M., Xueref-Remy, I., Kotthaus, S., Haefelin, M., and Ciais, P.: Sensi-  
531 tivity to the sources of uncertainties in the modeling of atmospheric CO<sub>2</sub> concentration within and in the vicinity of Paris, *Atmospheric  
532 Chemistry and Physics*, 21, 10 707–10 726, 2021.

533 Mahadevan, P., Wofsy, S. C., Matross, D. M., Xiao, X., Dunn, A. L., Lin, J. C., Gerbig, C., Munger, J. W., Chow, V. Y., and Gottlieb, E. W.: A  
534 satellite-based biosphere parameterization for net ecosystem CO<sub>2</sub> exchange: Vegetation Photosynthesis and Respiration Model (VPRM),  
535 *Global Biogeochemical Cycles*, 22, 2008.

536 Morrison, H., Thompson, G., and Tatarskii, V.: Impact of cloud microphysics on the development of trailing stratiform precipitation in a  
537 simulated squall line: Comparison of one-and two-moment schemes, *Monthly weather review*, 137, 991–1007, 2009.

538 Nerobelov, G., Timofeyev, Y., Smyshlyaev, S., Foka, S., Mammarella, I., and Virolainen, Y.: Validation of WRF-Chem model and CAMS  
539 performance in estimating near-surface atmospheric CO<sub>2</sub> mixing ratio in the area of Saint Petersburg (Russia), *Atmosphere*, 12, 387,  
540 2021.

541 Nogueira, T., Kamigauti, L. Y., Pereira, G. M., Gavidia-Calderon, M. E., Ibarra-Espinosa, S., Oliveira, G. L. d., Miranda, R. M. d., Vascon-  
542 cellos, P. d. C., Freitas, E. D. d., and Andrade, M. d. F.: Evolution of vehicle emission factors in a megacity affected by extensive biofuel  
543 use: results of tunnel measurements in São Paulo, Brazil, *Environmental Science & Technology*, 55, 6677–6687, 2021.

544 O'Dell, C., Connor, B., Bösch, H., O'Brien, D., Frankenberg, C., Castano, R., Christi, M., Eldering, D., Fisher, B., Gunson, M., et al.: The  
545 ACOS CO<sub>2</sub> retrieval algorithm–Part 1: Description and validation against synthetic observations, *Atmospheric Measurement Techniques*,  
546 5, 99–121, 2012.

547 Osterman, G., Eldering, A., Avis, C., Chafin, B., O'Dell, C., Frankenberg, C., Fisher, B., Mandrake, L., Wunch, D., Granat, R., et al.: Orbiting  
548 Carbon Observatory–2 (OCO-2) Data Product User's Guide, Operational L1 and L2 Data Versions 8 and Lite File Version 9, Version 1,  
549 Revision J., October 10, 2018, 2018.

550 Peiro, H., Crowell, S., Schuh, A., Baker, D. F., O'Dell, C., Jacobson, A. R., Chevallier, F., Liu, J., Eldering, A., Crisp, D., et al.: Four years  
551 of global carbon cycle observed from the Orbiting Carbon Observatory 2 (OCO-2) version 9 and in situ data and comparison to OCO-2  
552 version 7, *Atmospheric Chemistry and Physics*, 22, 1097–1130, 2022.

553 Raju, A., Sijikumar, S., Burman, P. K. D., Valsala, V., Tiwari, Y. K., Mukherjee, S., Lohani, P., and Kumar, K.: Very high-resolution Net  
554 Ecosystem Exchange over India using Vegetation Photosynthesis and Respiration Model (VPRM) simulations, *Ecological Modelling*,  
555 481, 110340, 2023.

556 Ramonet, M., Ciais, P., Apadula, F., Bartyzel, J., Bastos, A., Bergamaschi, P., Blanc, P., Brunner, D., Caracciolo di Torchiareolo, L., Calzo-  
557 lari, F., et al.: The fingerprint of the summer 2018 drought in Europe on ground-based atmospheric CO<sub>2</sub> measurements, *Philosophical  
558 Transactions of the Royal Society B*, 375, 20190513, 2020.

559 Rezende, C. L., Scarano, F. R., Assad, E. D., Joly, C. A., Metzger, J. P., Strassburg, B. B. N., Tabarelli, M., Fonseca, G. A., and Mittermeier,  
560 R. A.: From hotspot to hopespot: An opportunity for the Brazilian Atlantic Forest, *Perspectives in ecology and conservation*, 16, 208–214,  
561 2018.

562 Rocha, H. R. d., Freitas, H. C., Rosolem, R., Juárez, R. I., Tannus, R. N., Ligo, M. A., Cabral, O. M., and Dias, M. A.: Measurements of CO<sub>2</sub>  
563 exchange over a woodland savanna (Cerrado *Sensu stricto*) in southeast Brasil, *Biota Neotropica*, 2, 1–11, 2002.

564 SEEG: SEEG – Greenhouse Gas Emissions and Removals Estimation System, Climate Observatory, Tech. rep., seeg.eco.br, 2019.

565 SEEG: Contribuição da Mata Atlântica para a NDC brasileira: análise histórica das emissões de GEE e potencial de mitigação até 2050,  
566 Tech. rep., seeg.eco.br, 2021.

567 Segura-Barrero, R., Lauvaux, T., Lian, J., Ciais, P., Badia, A., Ventura, S., Bazzi, H., Abbessi, E., Fu, Z., Xiao, J., et al.: Heat and drought  
568 events alter biogenic capacity to balance CO<sub>2</sub> budget in south-western Europe, *Global Biogeochemical Cycles*, 39, e2024GB008163,  
569 2025.

570 Seo, M.-G., Kim, H. M., and Kim, D.-H.: Effect of atmospheric conditions and VPRM parameters on high-resolution regional CO<sub>2</sub> simula-  
571 tions over East Asia, *Theoretical and Applied Climatology*, 155, 859–877, 2024.

572 Seto, K. C., Güneralp, B., and Hutyrá, L. R.: Global forecasts of urban expansion to 2030 and direct impacts on biodiversity and carbon  
573 pools, *Proceedings of the National Academy of Sciences*, 109, 16083–16088, 2012.

574 Seto, K. C., Dhakal, S., Bigio, A., Blanco, H., Carlo Delgado, G., Dewar, D., Huang, L., Inaba, A., Kansal, A., Lwasa, S., et al.: Human  
575 settlements, infrastructure, and spatial planning, 2014.

576 Shimada, S., Ohsawa, T., Chikaoka, S., and Kozai, K.: Accuracy of the wind speed profile in the lower PBL as simulated by the WRF model,  
577 Sola, 7, 109–112, 2011.

578 Skamarock, W. C., Klemp, J. B., Dudhia, J., Gill, D. O., Liu, Z., Berner, J., Wang, W., Powers, J. G., Duda, M. G., Barker, D. M., et al.: A  
579 description of the advanced research WRF version 4, NCAR tech. note ncar/tn-556+ str, 145, 2019.

580 Souto-Oliveira, C. E., Marques, M. T., Nogueira, T., Lopes, F. J., Medeiros, J. A., Medeiros, I. M., Moreira, G. A., da Silva Dias, P. L.,  
581 Landulfo, E., and Andrade, M. d. F.: Impact of extreme wildfires from the Brazilian Forests and sugarcane burning on the air quality of  
582 the biggest megacity on South America, *Science of the Total Environment*, 888, 163 439, 2023.

583 Souza Jr, C. M., Z. Shimbo, J., Rosa, M. R., Parente, L. L., A. Alencar, A., Rudorff, B. F., Hasenack, H., Matsumoto, M., G. Ferreira, L.,  
584 Souza-Filho, P. W., et al.: Reconstructing three decades of land use and land cover changes in brazilian biomes with landsat archive and  
585 earth engine, *Remote Sensing*, 12, 2735, 2020.

586 Tewari, M., Chen, F., Kusaka, H., and Miao, S.: Coupled WRF/Unified Noah/urban-canopy modeling system, Near WRF Documentation,  
587 NCAR, Boulder, 122, 1–22, 2007.

588 Vara-Vela, A., Andrade, M. F., Kumar, P., Ynoue, R. Y., and Munoz, A. G.: Impact of vehicular emissions on the formation of fine particles  
589 in the Sao Paulo Metropolitan Area: a numerical study with the WRF-Chem model, *Atmospheric Chemistry and Physics*, 16, 777–797,  
590 2016.

591 Vara-Vela, A., de Fátima Andrade, M., Zhang, Y., Kumar, P., Ynoue, R. Y., Souto-Oliveira, C. E., da Silva Lopes, F. J., and Landulfo,  
592 E.: Modeling of atmospheric aerosol properties in the São Paulo metropolitan area: impact of biomass burning, *Journal of Geophysical*  
593 *Research: Atmospheres*, 123, 9935–9956, 2018.

594 Vara-Vela, A. L., Herdies, D. L., Alvim, D. S., Vendrasco, É. P., Figueroa, S. N., Pendharkar, J., and Reyes Fernandez, J. P.: A new predictive  
595 framework for Amazon forest fire smoke dispersion over South America, *Bulletin of the American Meteorological Society*, 102, E1700–  
596 E1713, 2021.

597 Vermote, E.: MODIS/Terra Surface Reflectance 8-Day L3 Global 500m SIN Grid V061, NASA EOSDIS Land Processes DAAC: Missoula,  
598 MT, USA, 2021.

599 Wilmot, T. Y., Lin, J. C., Wu, D., Oda, T., and Kort, E. A.: Toward a satellite-based monitoring system for urban CO2 emissions in support  
600 of global collective climate mitigation actions, *Environmental Research Letters*, 19, 084 029, 2024.

601 Zhang, L., Zhang, H., Li, Q., Wu, B., Cai, X., Song, Y., and Zhang, X.: Complexity of carbon dioxide flux in urban areas: A comparison with  
602 natural surfaces, *Science of the Total Environment*, 895, 165 115, 2023.

603 Zhang, Y., Dubey, M. K., Olsen, S., Zheng, J., and Zhang, R.: Comparisons of WRF/Chem simulations in Mexico City with ground-based  
604 RAMA measurements during the 2006-MILAGRO, *Atmospheric Chemistry and Physics*, 9, 3777–3798, 2009.